BNL-114379-2017-TECH
C-A/AP/590;BNL-114379-2017-IR

Re-visiting RHIC snakes: OPERA fields, n0 dance

F. Meot

September 2017

Collider Accelerator Department
Brookhaven National Laboratory

U.S. Department of Energy
USDOE Office of Science (SC), Nuclear Physics (NP) (SC-26)

DISCLAIMER

BNL-114379-2017-IR

C-A/AP/590
September 2017

Re-visiting RHIC snakes: OPERA fields, n_0 dance

**F. Meot, R. Gupta, H. Huang,
V. Ranjbar, G. Robert-Demolaize**

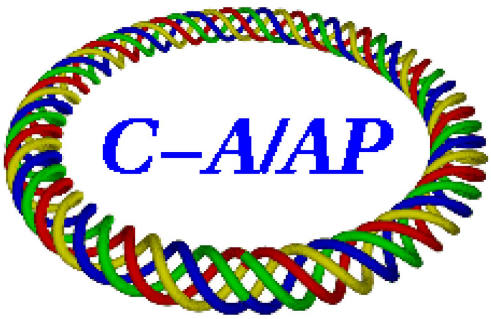

Collider-Accelerator Department
Brookhaven National Laboratory
Upton, N.Y. 11973

U.S. Department of Energy
Office of Science, Office of Nuclear Physics

DISCLAIMER

Re-visiting RHIC snakes : OPERA fields, $\vec{n}_0$ dance

F. Méot, R. Gupta, H. Huang, V. Ranjbar, G. Robert-Demolaize
Collider-Accelerator Department, BNL, Upton, NY 11973

September 22, 2017

Abstract

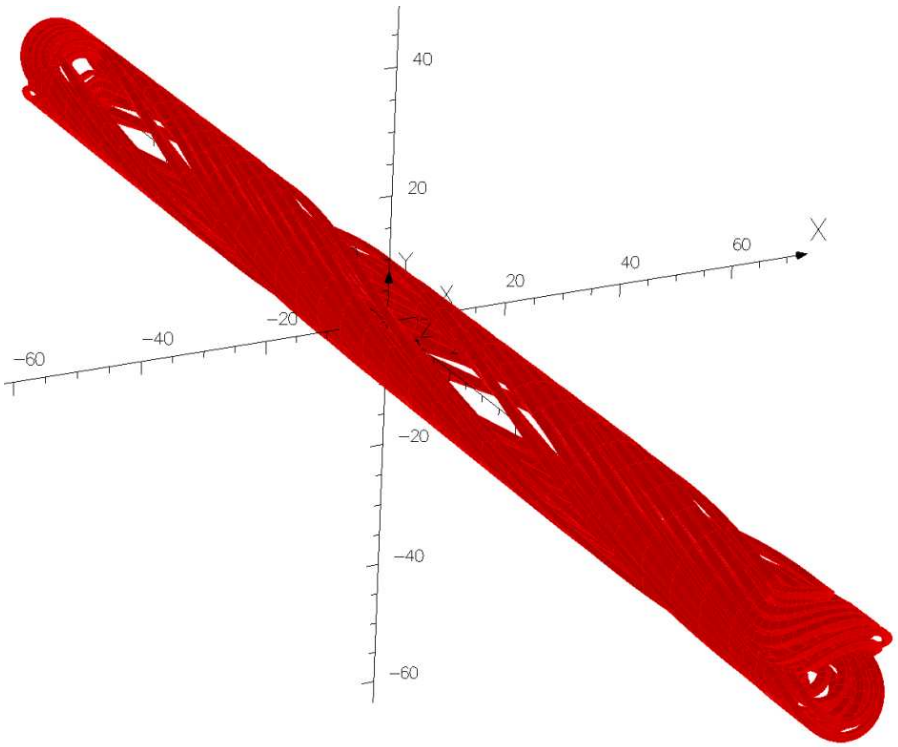

Tech. Note C-A/AP/590
BNL C-AD

Contents

1 Introduction

In this Tech. Note RHIC snakes and stable spin direction $\vec{n}_0(s)$ are re-visited, based on OPERA-computed field maps of the former. The numerical simulations so undertaken provide various outcomes regarding RHIC optics and spin dynamics, in relation with orbital and focusing effects resulting from the use of this realistic 3-D representation of the snakes. Note that details regarding the polarization context at RHIC complex, often implicit here, can be found in [1].

This work was undertaken in view of investigations following the observation, from polarization measurements performed during polarized proton Runs 11, 12, 13, 15, of a significant off-vertical tilt of the stable spin precession direction at the pC CNI polarimeter, in both Blue and Yellow rings, at 255 GeV [2]. This will be subject to a different Tech. Note.

RHIC helical snakes are discussed in detail in many publications over the period 1990s∼early 2000s [3], amongst which [4, 5] report on using a magnetic field map to represent a 360 degree twist helical dipole module of a snake that comprises four of those. The present work adopts the latter method, which required the production of 3D OPERA maps of the low-field and of the strong-field 360 deg. modules of a snake, as well as a complete field map of the 4-module 10 meter long snake. Having he possibility of using field maps has a series of outcomes, found in this Tech. Note, amongst other :

- comparison of particle and spin dynamics across a snake with theoretical expectations,
- computation of the transfer function from low- and strong-field helical dipole current to snake angles,
- realistic simulations of orbit and optics effects in RHIC,
- computation of the stable spin precession axis in RHIC, its dependence on energy, snake angle defects, etc.,
- comparison with polarization properties in RHIC using a theoretical local spin rotation.

Prior studies

Two of the earlier studies [4, 5] were based on the use of a 3D OPERA field map of the 2.4 m effective length helix to be constructed for RHIC. Yet they do not report on possible production of a full-snake 4-module field map, which we did produce and will investigate here. Also, some of the figures in [5] may not have explicitly distinguished between the low-field (maximum field in the 1.3 T region) and high-field (maximum field in the 4 T region) modes of operation of an helix. Both high-field and low-field cases have been subject to separate OPERA computations here, so accounting for saturation effects.

Finally, there is no earlier report of RHIC optics studies using RHIC snakes field maps, an aspect that we address here, which does require full-length, low- and high-field 3D field maps.

2 OPERA field maps

A principle scheme of RHIC snake is shown in Fig. 4. It is comprised of four identical, 2.4 m effective length, 360 degree right-handed twisted helix modules, low-field dipoles at both ends (maximum on-axis field denoted B_{low} in the text, common current I_{low}), a high-field pair in between (maximum on-axis field denoted B_{high} in the text, common current I_{high}), the field vector is vertical at the ends of the snake.

2.1 Single-map and 4-map snake models

Three OPERA 3D field maps have been computed in the present approach, based on a coil imported from earlier work [4], namely :

◇ A complete, 12 meter extent, single field map of the 10.6 meter snake (Fig. 1 - “full-snake” field map in the sequel), under two different versions, namely using either the ’nodal’ or the (reputedly more accurate) ’integral’ OPERA computation modes

$$\text{model4hel-a5-100A-322A-06-dec-2016-x-4\_4\_y-4\_4\_z-200\_1000-}\frac{\text{nodal.table}}{\text{integralPatched.table}} \tag{1}$$

Currents for this OPERA computation have been set to $I_{low} = 100$ A for the two low-field helix module at snake ends and $I_{high} = 322$ A for the two high-field ones in-between, values taken in the vicinity of the regular snake settings in RHIC in normal pp operation. Field shown in Fig. 5.

◇ A 3.6 meter extent field map of a single 2.4 meter helix module (Fig. 1), powered at low field, namely OPERA $I_{low} = 100$ A, field is shown in Fig. 6,

$$\text{model3a2a-x-4\_4\_y-4\_4\_z-180\_180-integral.table} \tag{2}$$

◇ Same field map, powered at high field, namely OPERA $I_{high} = 322$ A, field is shown in Fig. 7,

$$\text{model3a2a322a-x-4\_4\_y-4\_4\_z-180\_180-integral.table} \tag{3}$$

These OPERA maps are archived/available on C-AD computers at

/rap/lattice_tools/zgoubi/RHICZgoubiModel/snakeFieldMaps/161216_secondSet_inclSingleHelix

The goal in producing these different maps is to investigate and possibly validate (it will be the case) the assumption that an assemblage of 4 independent helix field maps yields equivalent field, particle motion and spin motion as the full-snake map (note that in the former case

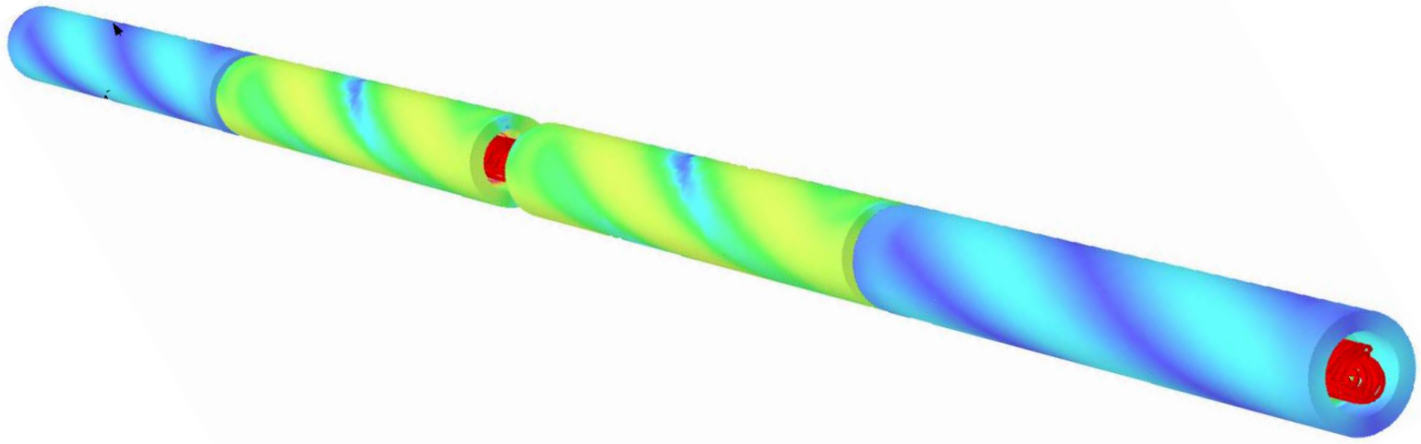

Figure 1: The 4-module full-snake model in OPERA.

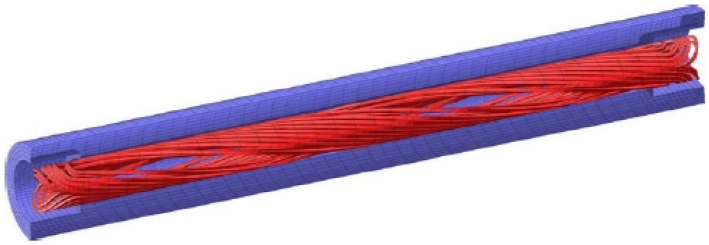

Figure 2: The 360^o-twist helix module model in OPERA.

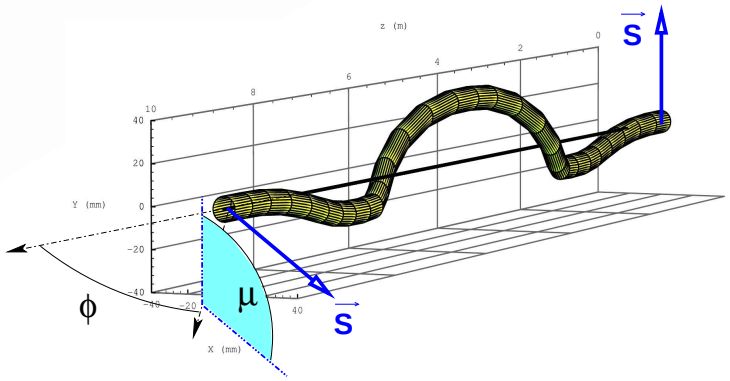

Figure 3: Spin rotation angle, μ, and apparent spin rotation axis at angle ϕ to the longitudinal direction.

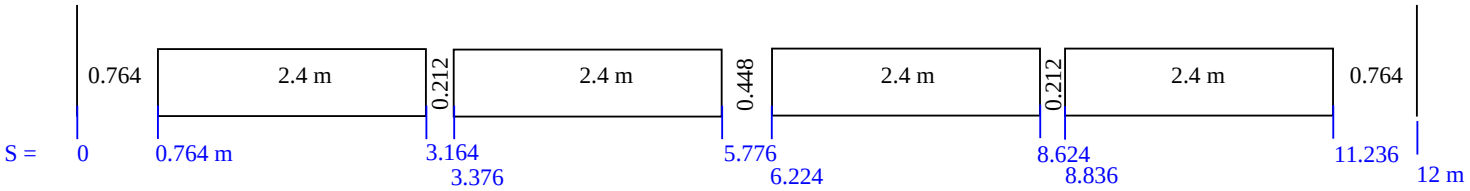

Figure 4: A sketch of RHIC snake layout in the OPERA field computation. Each 2.4 m long helix module is represented by a rectangle. The distances shown (meter) stem from the positioning of the center of the four magnets, in the OPERA field map frame.

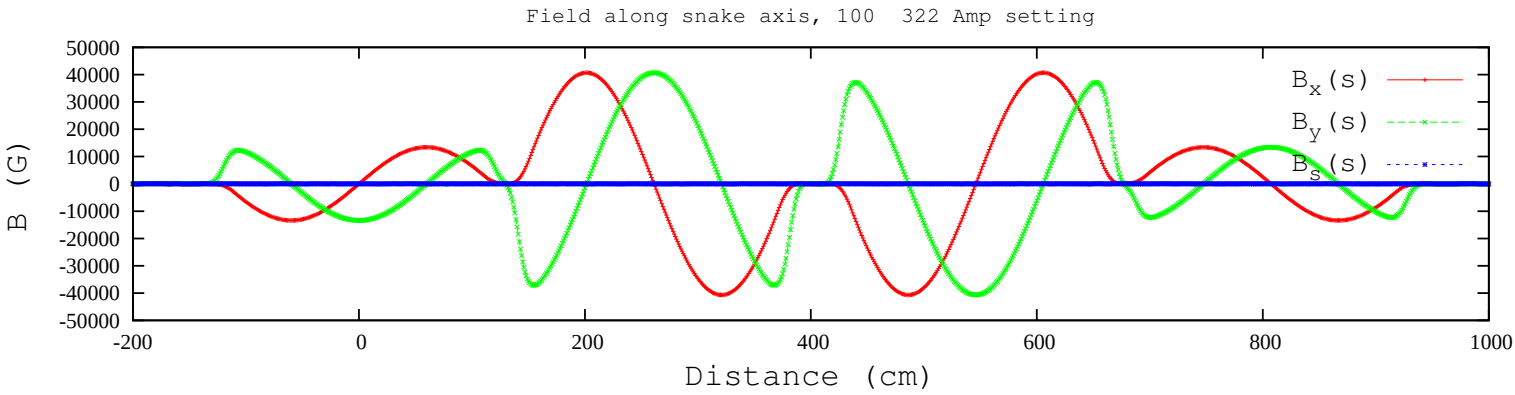

Figure 5: Field along the snake axis in the 4-module single-map OPERA model, 100 and 322 Amp OPERA current settings in respectively the two end and two central helix modules. Extreme on-axis field values come out to be, in the low-field helix module $B_x = 1.340$, $B_y = 1.340$, $|\vec{B}| = 1.340$ T. in the high-field helix module $B_x = 3.898$, $B_y = -3.896$, $|\vec{B}| = 3.903$ T.

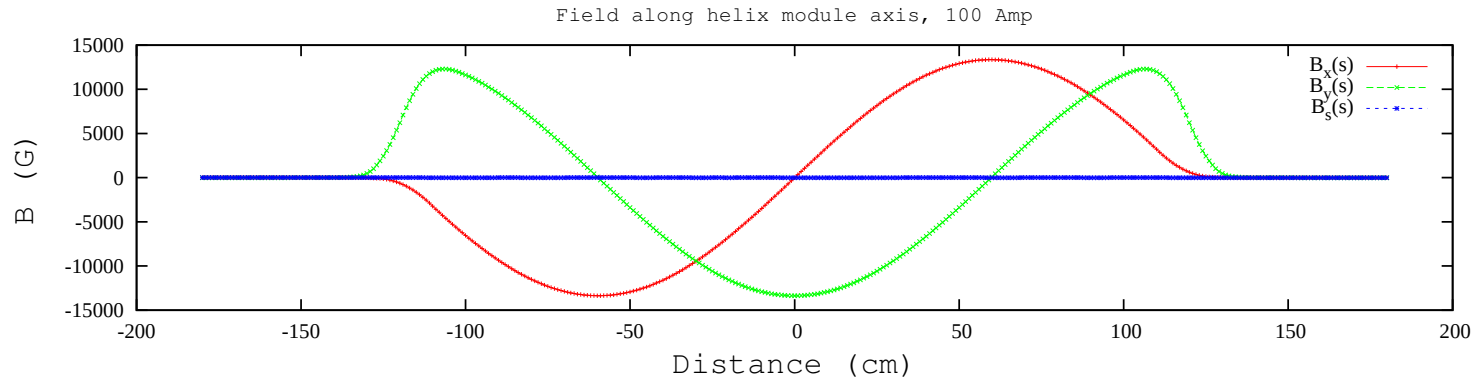

Figure 6: Field along the 360 degree helix axis, case of 100 A OPERA current. Extreme on-axis field values come out to be $B_x = 1.3359$, $B_y = -1.3364$, $|\vec{B}| = 1.3364$.

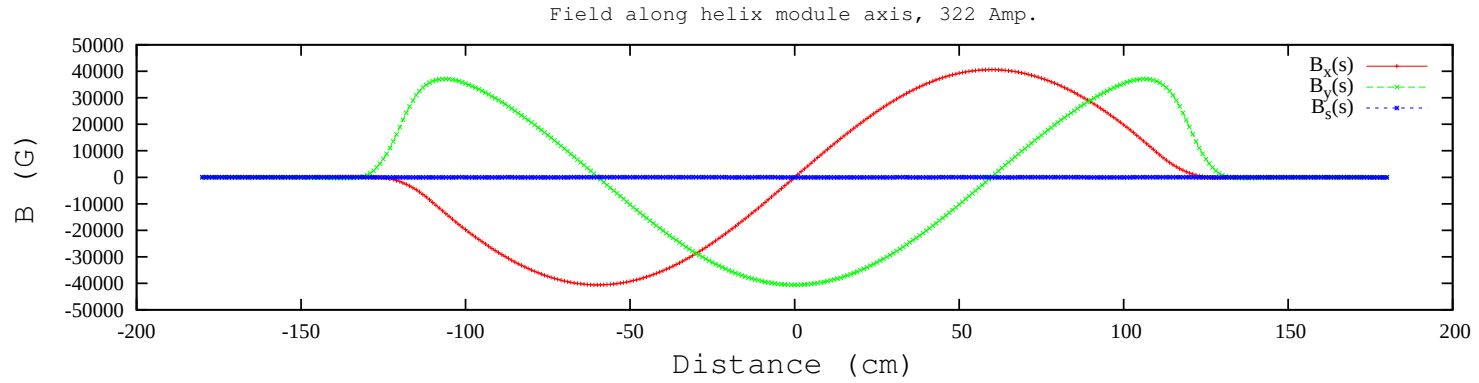

Figure 7: Field along the 360 degree helix axis, case of 322 A OPERA current. On-axis peak-field values come out to be $B_x = -4.0602$, $B_y = 4.0589$, $|\vec{B}| = 4.0677$, a not so small 4% difference compared to the complete 4-module snake, Fig. 5.

the magnetic field in the region between two field maps is taken as the linear superposition of the field from both maps). The interest if this hypothesis proves valid, at least in the current range of concern, I_{low} in the 100 A region and I_{high} in the 320 A region (it will, in a sufficient extent, see below), is in the flexibility that it brings of allowing independent optimization of I_{low} and I_{high}, for spin rotation angle and spin precession axis adjustments - it avoids the time costly computation of 12 m extent maps for different (I_{low}, I_{high}) settings. (Note that in the case that hypothesis would have proven not to hold, an alternate possibility would have been to interpolate in a small set of full-snake maps computed with different (I_{low}, I_{high}) couples.)

In brief (details $e.g.$ in [6]), RHIC snake is made up of four identical right-handed helical dipole magnets (right-handed chirality : the field is seen rotating clockwise when proceeding along the helix axis). In addition,

- the magnetic field is vertical at the entrance and exit of the snake,
- its component (respectively B_y) B_x is symmetric with respect to the (resp. vertical plane at) center of the snake.

The spin precession axis in this system is in the horizontal plane, and the orbit bump the system causes is closed.

A note in passing : it is necessary to know the exact position of the dipole in the field map frame, for its correct positioning in RHIC lattice, Appendix A discusses that point. A small mis-positioning can only have negligible effect on optics anyway, and it does not have any on spin rotation.

2.2 On the single-map full-snake model

The full-snake field map has been computed with $(I_{low}, I_{high}) = (100A, 322A)$ low-field and high-field helix currents respectively. This results in the field components displayed in Fig. 5.

It comes out, see Tab. 1, that the current-to-field correspondence in the two high-field helix modules *is not the same* as in the case of a single high-field helix. As a result the normalization rule is actually different from what Tab. 1 provides - and remains to be determined... This might justify an iteration in OPERA computing, so to get the optimal 4-module single-map current setting ("optimal" in the sense $\mu = 180$ deg, $\phi = \pm 45$ deg, at 255 GeV).

Regarding tracking simulations : it is doable by splitting the 12 meter extent field map in 4 distinct numerical integration regions ($+\mathrm{B_{low}}/-\mathrm{B_{high}}/+\mathrm{B_{high}}/-\mathrm{B_{low}}$), to independently adjust the fields to get the optimal setting (yielding $\mu = 180$ deg, $\phi = -45$ deg at 255 GeV). Ray-tracing shows that, bringing the 'splitted snake' B_{low}, B_{high} values to the 1-map model B_{low} and B_{high} ones requires scaling the splitted map by respectively 0.997 and 1.042, Fig. 8. These scaling factor values happen to coincide with the ratio, respectively, 1.336/1.340, 4.060/3.900, as field extrema are essentially insensitive to the helical trajectory excursion across the magnets.

Spin tracking also shows (Sec. 3) that this scaling results in quasi-identical spin rotation and rotation axis orientation, from both four single-helix maps or one 4-module full-snake map models.

From what it can be concluded that the 4-map model is convenient with marginal effect on actual current values (see Tab. 1).

2.3 Field normalization

Magnetic field measurements have established the correspondence from feed current $I_{low},\ I_{high}$ to maximum field amplitude $B_{low},\ B_{high}$ along the 360 degree helix axis, in the case of a single helix. This allows to account for field saturation as current increases, so giving a correspondence between OPERA and real-life currents. This is displayed in Fig. 8, together with the case of the current settings (100 A and 322 A) in the OPERA map computations.

Note that this correction is only valid to the extent that a single, high-field helix is assumed to behave in the same manner as when located in the central region in the snake. As a matter of fact, the 4-module single-map OPERA computation shows that this is not exactly the case. This is discussed further in Sec. 2.2.

Differences are small anyway : at 100 and 322 Amp, the measured low- and high-field in the magnet prototype is respectively 1.337 T and 4.066 T (interpolated from the data list in Tab. 1), whereas for these very current values OPERA yields respectively, either 1.340 T and 3.903 T in the case of the 4-module full-snake (Fig.5), or 1.336 T and 4.068 T, single helix case (Figs.6, 7).

2.4 Theory

These OPERA outcomes have been subjected to various comparisons with basic theoretical expectations [7, 8, 9], as follows.

• The transverse field components along the helical trajectory (ignoring end field fall-off effects) satisfy, to order zero in x, y excursions (respectively, the horizontal and vertical distance to the helix axis) [7],

$$\begin{cases} B_x = B_0 \cos(ks) \\ B_y = B_0 \sin(ks) \end{cases} \tag{4}$$

with $k = 2\pi/\lambda$ the helical coil pitch (here, $\lambda = 2.4$ m, $k = 2.618\ \mathrm{m}^{-1}$), s the distance along the helix axis, B_0 the peak transverse field value.

To second order in x, y and including the longitudinal component,

$$\begin{cases} B_x/B_0 = \cos(ks)(1 + \frac{k^2}{8}(3x^2 + y^2)) + \frac{k^2}{4} xy \sin(ks) \\ B_y/B_0 = \sin(ks)(1 + \frac{k^2}{8}(x^2 + 3y^2)) + \frac{k^2}{4} xy \cos(ks) \\ B_l/B_0 = -k(x \sin(ks) - y \cos(ks)) \end{cases} \tag{5}$$

Given the radial excursions of concern here, namely $x,\ y$ in 2 cm range at lower energy (see Figs. 9, 11), while $k^2/8 \approx 1$, the non-linear terms have negligible contribution to the field. As a consequence the transverse field components do not depend on the energy, this is illustrated in Fig. 12. Such is not the case for the longitudinal field component B_l which is of first order in x, y.

Table 1: Left two columns : current to peak-field correspondence, from field measurements of a 360 deg twist helix ; values between parenthesis are from interpolation ; boxed values are optimum ones, as of this study, in the single-map full-snake model. Col. 3 : low-field and high-field current values in the separate, low-field and high-field helix modules. Col. 4 : current values in the single-map, full-snake OPERA map model. In cols. 3 and 4, (*)'ed current values are the optimal settings, they yield $\mu = 180$ deg, $\phi = \pm 45$ deg snake angles at 250 GeV. OPERA currents in cols. 3, 4 are placed vis-à-vis B(T) field values to be understood for the circumstance as the OPERA ones.

I[A]	B[T]	I[A]	
MEASURED		—- OPERA —-	
		4-MAP model	1-MAP model
(93.57)	(1.251)	*93.6	
(94.25)	(1.260)		*94.3
(99.95)	(1.336)	100	
(100.25)	(1.340)		100
102.64	1.372		
143.82	1.921		
185	2.465		
226.19	2.994		
246.78	3.246		
257.08	3.367		
267.4	3.485		
277.7	3.598		
288	3.712		
298.3	3.822		
(305.8)	3.9		322
308.6	3.929		
318.89	4.034		
(321.45)	(4.060)	322	
(322.25)	(4.068)		*322.7
(322.45)	(4.070)	*322.9	
329.18	4.138		
339.48	4.240		
349.76	4.341		
370.37	4.539		

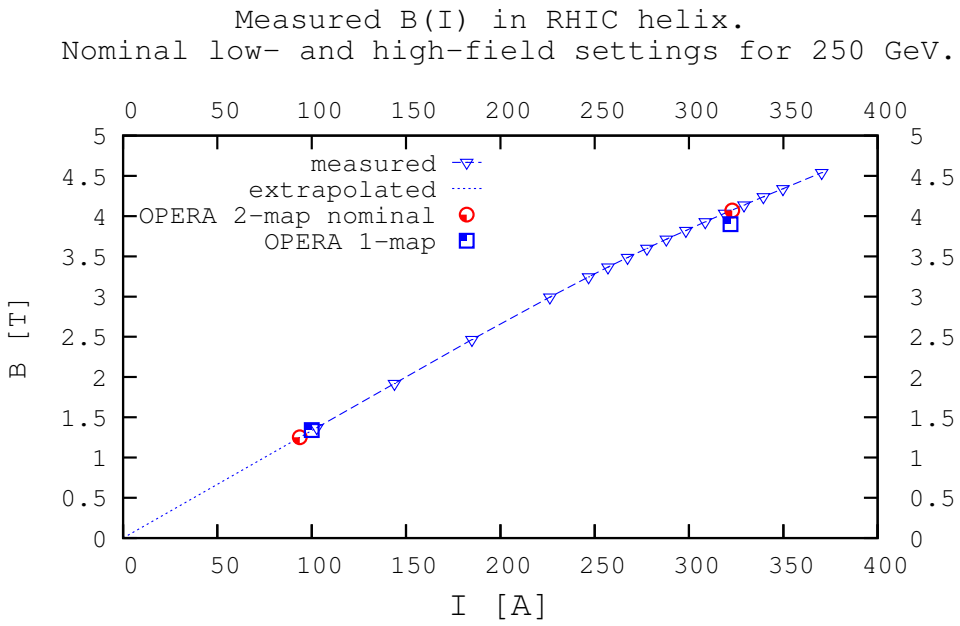

Figure 8: Field normalization, a rule to apply to the OPERA field maps. Blue triangles : from field measurements in a 360^o twist helical dipole. Red circles : nominal current settings in RHIC and corresponding field in the 4-map OPERA model, with OPERA currents (I_{low}, I_{high}) set to $(93.6, 322.9)$ (as in Fig. 16). Blue squares : from the single-map full-snake model, with OPERA currents (I_{low}, I_{high}) set to $(100A, 322A)$.

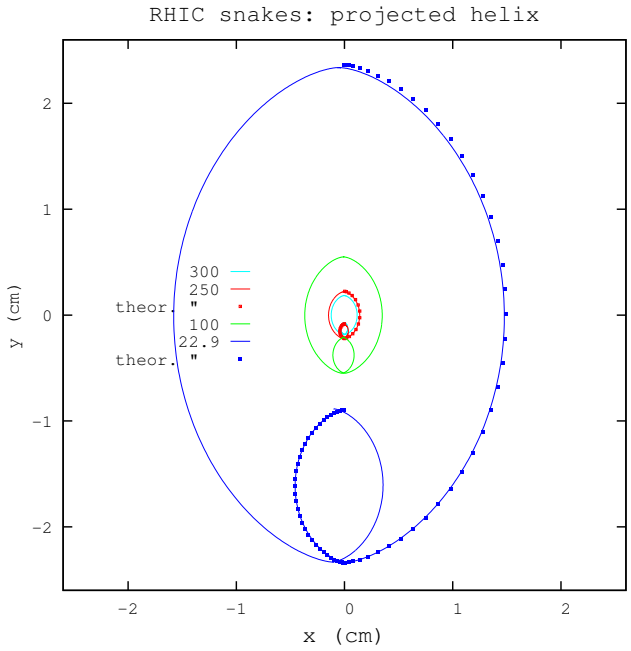

Figure 9: Projection of the (non-circular) helical motion in the transverse plane (smaller excursion is in the low-field magnet), from theory at 22.9 and 250 GeV (solid lines, Eq. 6) and from the 4-map snake model at 23, 100, 250 and 300 GeV (markers). Case of 250 GeV-nominal OPERA peak-field values $B_{low} = 1.251$ T, $B_{high} = 4.070$ T.

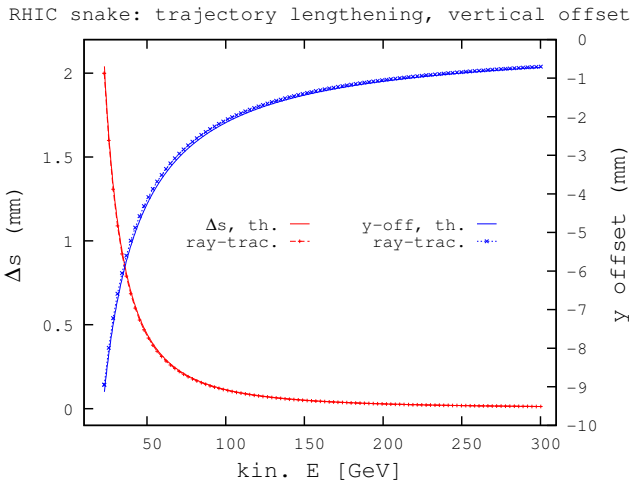

Figure 10: Energy dependence of the orbit lengthening (left vertical axis) and vertical orbit off-centering at snake entrance (right), from theory (solid lines, Eqs. 8 and 9, respectively) and from ray-tracing, optimal field 4-map model (markers).

◇ **In the three plots below, OPERA current signs in the four modules are +/-/+/- respectively**

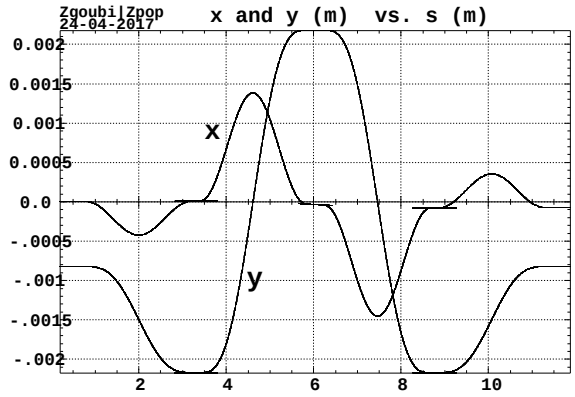

Figure 11: x and y coordinates across the four-map OPERA model ($G\gamma = 487$) (the short segments in the intermediate regions between the modules are an artifact of the ray-tracing). Note that the in and out horizontal motion coordinates differ slightly (this difference reaches 1 mm at 23 GeV), this is a source of an horizontal closed orbit effect, in RHIC. The excursion shrinks with increasing energy (Eq. 6 and Fig. 9).

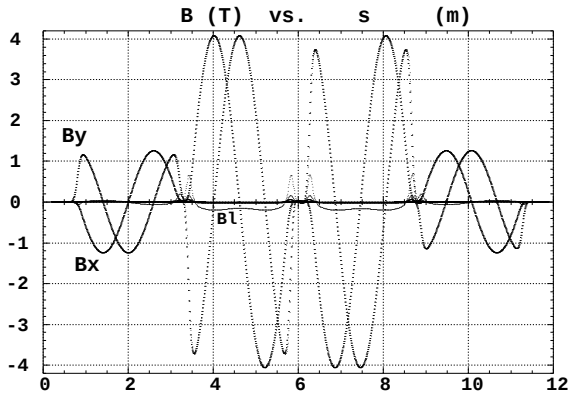

Figure 12: B_x, B_y, B_l components of the magnetic field experienced along the helical trajectories, at 23, 100, 250 and 300 GeV superimposed. $B_{x,y}$ are essentially independent of the energy as expected, B_l, weak anyway, is not (Eq. 5).

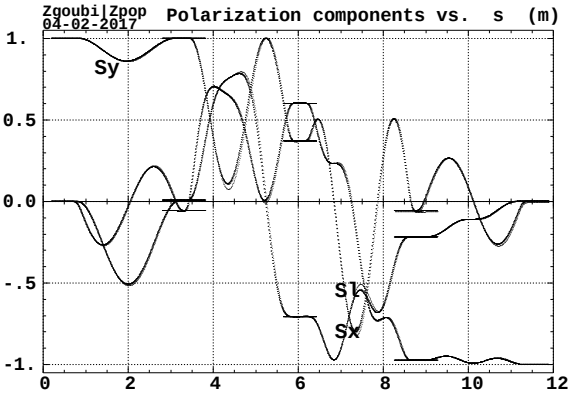

Figure 13: Evolution of the spin components along the helical trajectories of Fig. 11 (nominal peak-field setting $B_{low} = 1.251$ T, $B_{high} = 4.070$ T). Four energies represented : 23, 100, 250 and 300 GeV, $S_{x,y,l}$ are essentially independent of energy, as expected from that very property of $B_{x,y}$.

Table 2: Trajectory lengthening (Δs), vertical amplitude of the trajectory in the low- and high-field helix modules (Δy), and vertical orbit centering offset at snake entrance ($y_{\rm off}$), case of the 4-map snake model with optimal fields B_{low}=1.251 T and B_{high}=4.070 T (these yield $\mu = 180$ deg, $\phi = \pm 45$ deg at 250 GeV).

Kin. E	GeV	22.87	100	250	300
$B\rho$	T.m	79.3668	336.7	837.0	1003.8
Δs	mm	2.02	0.112	0.018	0.013
$\Delta y_{\rm low}$	mm	14.4	3.4	1.4	1.1
$\Delta y_{\rm high}$	mm	47	11.1	4.5	3.7
$y_{\rm off}$	mm	9	2.1	0.86	0.72

• The particle motion is a non-circular helix with coordinates (taking the origin at $s = 0$)

$$\left\{ \begin{array}{l} x = x_0 + \frac{B_0}{k^2 B\rho}\left[\cos(ks+\alpha) - \cos(\alpha)\right] + \left[x'_0 + \frac{B_0}{kB\rho}\sin(\alpha)\right]s \\ y = y_0 + \frac{B_0}{k^2 B\rho}\left[\sin(ks+\alpha) - \sin(\alpha)\right] + \left[y'_0 - \frac{B_0}{kB\rho}\cos(\alpha)\right]s \end{array} \right. \stackrel{\begin{array}{c} x'_0=y'_0=0 \\ \alpha=0 \end{array}}{\longrightarrow} \left\{ \begin{array}{l} x = x_0 + \frac{B_0}{k^2 B\rho}\left[\cos(ks) - 1\right] \\ y = y_0 + \frac{B_0}{k^2 B\rho}\sin(ks) - \frac{B_0}{kB\rho}s \end{array} \right. \quad (6)$$

with $x_0,\ ,x'_0,\ y_0, y'_0$ the initial coordinates, α the angle of the field to the vertical at entrance ($\alpha = 0$ here), $B\rho$ the particle rigidity. The vertical amplitude of the motion over the extent λ of an helical dipole is

$$\Delta y = \frac{B_o \lambda}{kB\rho} \quad (7)$$

which yields $\Delta y_{\rm low}$ and $\Delta y_{\rm high}$ that agree with ray-tracing outcomes given in Tab. 2.

• Trajectory lengthening can be derived from the Eqs. 6 with appropriate approximations, and writes [8]

$$\Delta s = \frac{\lambda^3}{2\pi^2}\frac{B_{low}^2 + B_{high}^2}{B\rho^2} = \frac{\lambda^3 c^2}{2\pi^2 M}\frac{B_{low}^2 + B_{high}^2}{\gamma^2 - 1} \quad (8)$$

with $M = 938.272 \times 10^6$ eV/c^2 the particle mass and γ its Lorentz relativistic factor, c the velocity of light. Trajectory lengthening is apparent in Fig. 9, its energy dependence and comparison with ray-tracing outcomes are displayed in Fig. 10.

• The vertical orbit offset at entrance of the snake, necessary to center the helical trajectory on the high-field helix axis, is approximately

$$y_{\rm off} \approx \frac{1}{2}\Delta y_{\rm high} - \Delta y_{\rm low} = \frac{B_{high} - 2B_{low}}{2kB\rho}\lambda \quad (9)$$

with $\Delta y_{\rm high}$, $\Delta y_{\rm low}$ the elevation in respectively the high- and low-field helix (Eq. 7). This energy dependence is displayed in Fig. 10. Ray-tracing outcomes are in accord, particular values for some RHIC energies are given in Tab. 2.

• The spin transport matrix $[M_{ij}]$ through the snake provides spin rotation μ and spin rotation axis (a_s, a_x, a_y),

$$\mu = \mathrm{acos}((\mathrm{Trace}(M) - 1)/2), \quad (a_s, a_x, a_y) = (M_{32} - M_{23}, M_{13} - M_{31}, M_{21} - M_{12})$$

Here it is obtained by tracking three initially orthogonal polarization conditions, along the reference on-momentum particle motion helix.

In the ring case, one-turn mapping (see for instance Tab. 4),

$$Q_{\rm sp} = \text{spin tune} = \mu \,/\, 2\pi$$

2.5 RHIC snake model

A conclusion of these investigations and comparisons is that, representing the snake by using independent low-field and high-field helix OPERA maps computed in respectively $I_{low} = 100A$ and $I_{high} = 322A$ region, which is close to nominal, does function : once the field in the independently computed low-field and high-field helix modules on the one hand, and the field in the 4 segments of the splitted single-map of the full-snake on the other hand, are normalized to the same maximum low-field and high-field amplitudes, then both models yield marginally different fields, trajectories, and spin motion along the snake (the cross-talk pointed out in Sec. 2.2 is weak and has negligible effect). Details can be found in App. B.

The key ingredients are the appropriate normalizations for the B_{low} and B_{high} helix fields, and these are eventually determined from, on the one hand the requested spin motion ($180^{\rm o}$ rotation angle and $\pm 45^{\rm o}$ precession axis orientation), on the other hand the $B \leftrightarrow I$ transfer functions as discussed above.

Note that, in the matter of flexibility of the modelling, the previous section indicates that the independent B_{low} and B_{high} helix modules can be represented indifferently by

- either the low-field and high-field segments extracted from the 12 meter extent full-snake field map,
- or the independent OPERA field maps of the low-field and high-field helix modules,

with specific field scaling factors in each case.

Four-map model

To conclude this section, Fig. 11 gives the trajectory coordinates across the snake in the 4-map model at 255 GeV, Figs. 12 and 13 give respectively the field experienced and spin motion in the 23 to 300 GeV energy range (computation is pushed to 300 GeV to include the 275 GeV region as envisaged in the frame of eRHIC EIC project [10]).

The vertical position of the helical trajectory at entrance into the snake ($i.e.$, into the low-field helix) is such as to center the excursion in the high-field helix, of the order of half the maximum helix diameter (Eq. 6). Note that the horizontal position at the exit of the snake differs slightly from zero, its value at the entrance. These orbit effects and their compensation in RHIC result in a slightly non-vertical stable spin direction $\vec{n}_0$ around the ring (this is addressed in Sec. 3.3).

These maps are used with the field scaled linearly to ensure optimal spin angles, namely, here the OPERA current is scaled to bring (B_{low}, B_{high}) in the $(1.26T, 4.07T)$ region so to yield 180 degrees spin rotation and precession axis at $\pm$45 degrees to the longitudinal axis at 250 GeV in the isolated snake, Fig. 13, this is discussed further in the next section.

3 Spin rotation

3.1 Full-snake single OPERA map model

Figure 14 displays a scan of the spin rotation angle μ and spin precession axis orientation ϕ, over the energy range 23-250 GeV, in the single-map snake model, case of respectively 'integral' and 'nodal' OPERA computation mode (field map names in Eq. 1).

OPERA current setting in this field map is $(I_{low}, I_{high}) = (100A, 322A)$ (respectively +/-/+/- and -/+/-/+ current sign series in the successive 4 helical dipoles for $\phi = -45^o$ and $\phi = +45^o$ from the longitudinal axis), so yielding on-axis peak-field value $(B_{low}, B_{high}) = (1.34T, 3.90T)$ as shown in Tab. 1. In this scan, the helical trajectory is maintained centered on the axis in the high-field helix modules at all currents (by changing the entrance y value), as shown in Fig. 14.

In order to assess the scaling needed on B_{low}, B_{high} for recovering the required 180deg/45deg spin rotation parameters in the 250 GeV region, the 12 meter extent map has been splitted into four independent motion integration sections covering respectively the four low-field and high-field regions, about 3 meter long each. The necessary scaling on fields comes out to be 0.94504 and 1.0441, respectively, meaning (see Tab. 1 which compares the various configuration),

$$\begin{gathered}\textbf{optimal maximum fields :}\ B_{low} = 1.26\ T,\ B_{high} = 4.068\ T,\\ \text{OPERA currents : } I_{low} = 94.3\ A,\ I_{high} = 322.7\ A\\ \text{real-life currents : } I_{low} = 94.25\ A,\ I_{high} = 322.25\ A,\end{gathered}$$

Note that maximum on-axis field values found, $B_{low} = 1.260\ T$ and $B_{high} = 4.068$ are close to the 4-map model ones, see Sec. 3.2. The resulting energy-dependence of ϕ (axis) and μ (rotation) angles in this "single-map, splitted" model is displayed in Fig. 15.

3.2 Four-map snake model

Figure 16 displays a scan of the spin rotation angle and spin precession axis orientation, over the energy range 23-300 GeV, in the 4-map snake model with low-field and high-field helix modules independently scaled to provide $(\mu, \phi) = (180\text{deg}, 45\text{deg})$. These results are practically invariant with the current sign series in the successive 4 helical dipoles, respectively +/-/+/- and -/+/-/+ for $\phi = -45^o$ and $\phi = +45^o$.

These nominal $(\mu, \phi) = (180\text{deg}, 45\text{deg})$ values in the 250 GeV region are obtained with 0.936419 A and 1.002754 scaling on respectively the $I_{low} = 100$ A and $I_{high} = 322$ A OPERA maps (field map names in Eq. 2, 3), meaning (see Tab. 1 which compares the various configuration),

$$\begin{gathered}\textbf{optimal maximum fields :}\ B_{low} = 1.251\ T,\ B_{high} = 4.070\ T,\\ \text{OPERA currents : } I_{low} = 93.6\ A,\ I_{high} = 322.9\ A\\ \text{real-life currents : } I_{low} = 93.57\ A,\ I_{high} = 322.45\ A,\end{gathered}$$

During the scan the helical trajectory is maintained centered on the axis in the high-field helix module at all currents (by changing entrance y value), in the manner shown in Fig. 9.

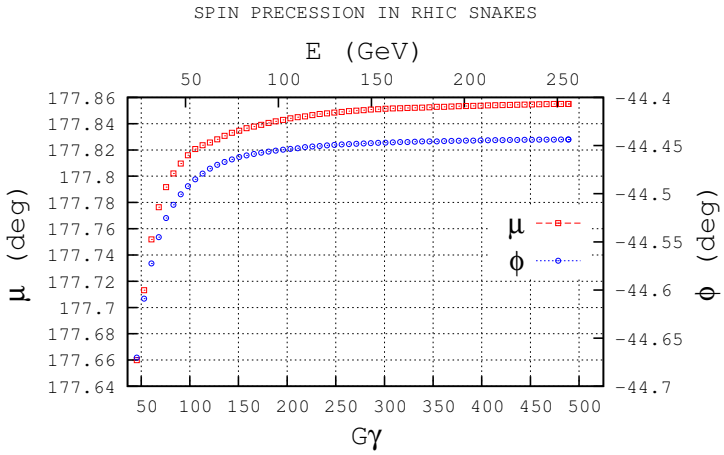

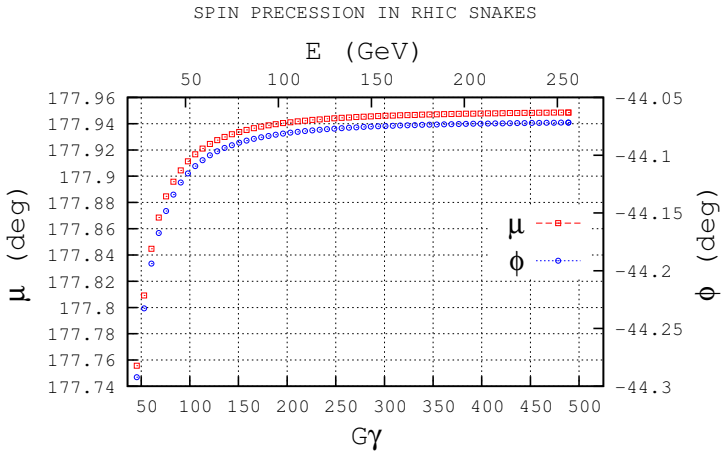

Figure 14: Single-map full-snake OPERA model, native current setting $(I_{low}, I_{high}) = (100A, 322A)$ (using field maps listed in Eq. 1). Left : case of 'nodal' OPERA computation mode, right : case of 'integral' mode, reputedly more accurate.

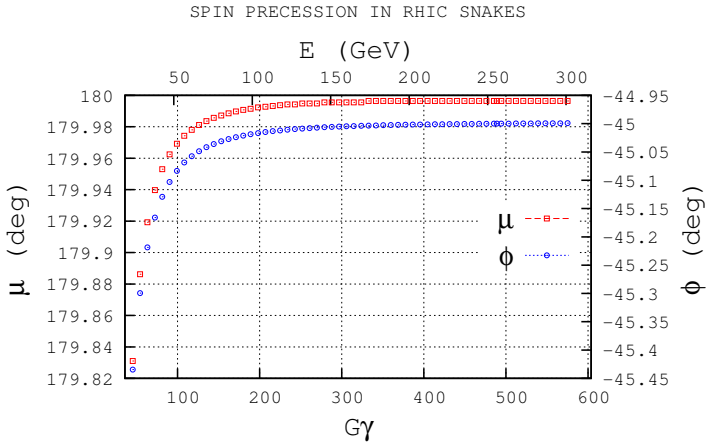

Figure 15: Optimized single-map full-snake OPERA model ("integralPatched.table", *i.e.*, that of Fig. 14-right used splitted into 4 segments for independent low- and high-field scaling), OPERA currents scaled to $I_{low} = 94.3\ A$, $I_{high} = 322.7\ A$ (real-life currents : $I_{low} = 94.25\ A$, $I_{high} = 322.25\ A$ after Tab. 1).

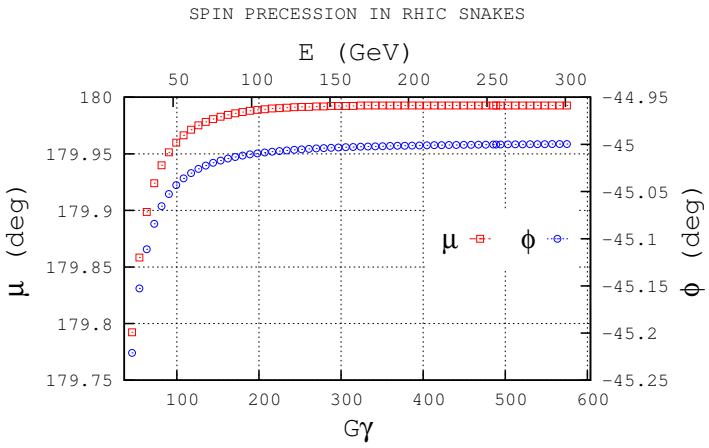

Figure 16: Optimized 4-map OPERA model (using field maps listed in Eqs. 2, 3), OPERA currents scaled to $I_{low} = 93.6\ A$, $I_{high} = 322.9\ A$ (real-life currents : $I_{low} = 93.57\ A$, $I_{high} = 322.45\ A$ after Tab. 1).

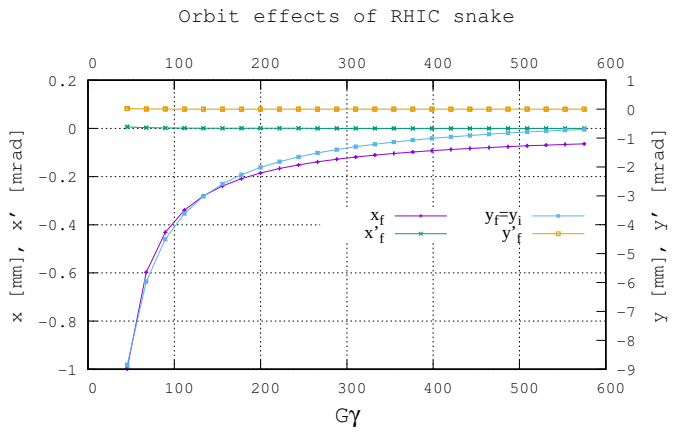

Figure 17: A scan in energy of orbit effects at the snake. Left vertical axis : given $x_i = 0$ and $x'_i = 0$ incoming orbit, one gets $x'_f \approx 0$ whereas x_f varies from -1 mm at $G\gamma = 45.5$ to ~ -0.1 mm at $G\gamma$ in the 250 GeV region. Right vertical axis : upon centering of the vertical orbit on the high-field snake axis, with initial angle $y'_i = 0$, coordinates y_i (entrance) and y_f at the exit of the snake remain equal while $y'_f \approx 0$, thus the snake induces negligible vertical orbit defect.

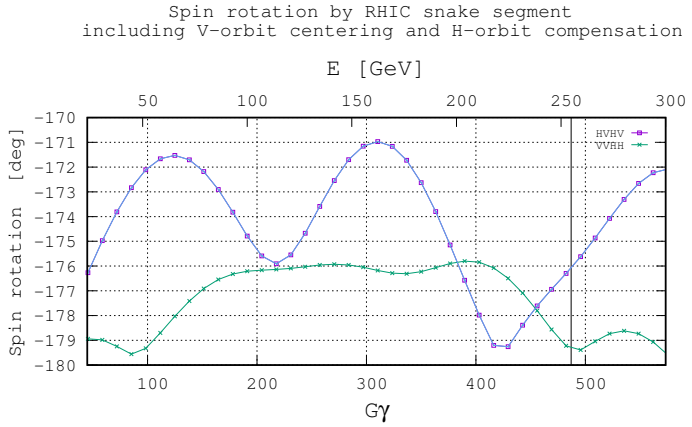

Figure 18: A scan in energy of spin rotation in the snake+correctors beam line segment [BI9_QF11 - BI9_TV4] in RHIC Blue, given vertical incoming spin and helical trajectory vertically centered on high-field helix axis, with nominal snake currents (*i.e.*, for $(\mu,\phi) = (180, \pm 45)$ degree at 250 GeV, yielding $\mu = 179.79$, $\phi = \pm 45.22$ at $G\gamma = 45.5$). The vertical bar at $G\gamma = 487$ is Run 17 store energy. Two corrector schemes for orbit zero-ing are scanned : HVHV and VVHH, the latter yields closest approach to 180^o rotation, the former yields a 4 degree spin rotation defect.

Table 3: This table gives the dependence of ϕ (axis orientation) and μ (spin rotation) angles on I_{low} and I_{high} currents (in Ampère). It has been generated using the 4-map snake model (field maps listed in Eqs. 2, 3, also the model that yields the $G\gamma$ dependence of Fig. 16). The same field maps are used of course for "SNAKE 1" and "SNAKE 2", their settings in RHIC ring only differ by I_{low} and I_{high} current signs being permuted : current signs +/-/+/- in SNAKE 1, -/+/-/+ in SNAKE 2. Currents are OPERA's, they can be converted to real-life (a marginal effect) using Tab. 1. In a direct triedra (s, x, y) attached to the snake, with s along the snake axis, ϕ (which is contained in the (s,x) plane) is counted with respect to the s axis, positive counter-clockwise.

• ϕ versus I_{low}, I_{high} in SNAKE 1 (currents : +/-/+/-) and SNAKE 2 (-/+/-/+)

Ilow: / Ihigh	60.0	64.0	68.0	72.0	76.0	80.0	84.0	88.0	92.0	96.0	100.0	104.0	108.0	112.0	116.0	120.0	124.0	128.0	132.0	136.0	140.0
286.0	145.8	147.2	147.5	147.8	148.1	148.5	148.9	149.4	149.8	150.3	150.8	151.4	151.9	152.5	153.1	-26.2	-25.6	-24.9	-24.1	-23.4	-22.6
290.0	144.4	145.7	146.0	146.3	146.7	147.1	147.5	147.9	148.3	148.8	149.3	149.9	150.4	151.0	151.6	-27.8	-27.1	-26.4	-25.7	-24.9	-24.1
294.0	143.0	144.2	144.5	144.9	145.2	145.6	146.0	146.4	146.8	147.3	147.8	148.3	148.9	149.5	-29.9	-29.3	-28.7	-28.0	-27.3	-26.5	-25.8
298.0	141.5	142.7	143.0	143.3	143.7	144.0	144.4	144.8	145.3	145.7	146.2	146.7	147.3	-32.1	-31.5	-30.9	-30.3	-29.6	-28.9	-28.2	-27.4
302.0	139.9	141.2	141.5	141.8	142.1	142.5	142.8	143.2	143.7	144.1	144.6	145.1	-34.3	-33.8	-33.2	-32.6	-31.9	-31.3	-30.6	-29.9	-29.1
306.0	138.4	139.6	139.9	140.2	140.5	140.9	141.2	141.6	142.1	142.5	143.0	143.5	-36.0	-35.4	-34.8	-34.2	-33.6	-33.0	-32.3	-31.6	-30.8
310.0	136.8	138.0	138.2	138.5	138.9	139.2	139.6	140.0	140.4	140.8	141.3	-38.2	-37.7	-37.1	-36.5	-36.0	-35.3	-34.7	-34.0	-33.3	-32.6
314.0	135.1	136.3	136.6	136.9	137.2	137.5	137.9	138.3	138.7	139.1	-40.4	-39.9	-39.4	-38.9	-38.3	-37.7	-37.1	-36.5	-35.8	-35.1	-34.4
318.0	133.5	134.6	134.9	135.2	135.5	135.8	136.2	136.6	137.0	137.4	-42.1	-41.7	-41.1	-40.6	-40.1	-39.5	-38.9	-38.2	-37.6	-36.9	-36.2
322.0	131.8	132.9	133.2	133.4	133.8	134.1	134.4	134.8	135.2	-44.4	-43.9	-43.4	-42.9	-42.4	-41.9	-41.3	-40.7	-40.1	-39.4	-38.8	-38.1
326.0	130.1	131.1	131.4	131.7	132.0	132.3	132.7	133.0	-46.6	-46.1	-45.7	-45.2	-44.7	-44.2	-43.7	-43.1	-42.5	-41.9	-41.3	-40.6	-39.9
330.0	128.3	129.4	129.6	129.9	130.2	130.5	130.9	131.2	-48.4	-48.0	-47.5	-47.0	-46.6	-46.0	-45.5	-45.0	-44.4	-43.8	-43.1	-42.5	-41.8
334.0	126.5	127.6	127.8	128.1	128.4	128.7	129.0	-50.6	-50.2	-49.8	-49.4	-48.9	-48.4	-47.9	-47.4	-46.8	-46.3	-45.7	-45.0	-44.4	-43.7
338.0	124.7	125.7	126.0	126.2	126.5	126.8	127.2	-52.5	-52.1	-51.7	-51.2	-50.8	-50.3	-49.8	-49.3	-48.7	-48.1	-47.5	-46.9	-46.3	-45.6
342.0	122.9	123.9	124.1	124.4	124.7	125.0	-54.7	-54.3	-53.9	-53.5	-53.1	-52.7	-52.2	-51.7	-51.1	-50.6	-50.0	-49.4	-48.8	-48.2	-47.5
346.0	121.0	122.0	122.2	122.5	122.8	123.1	-56.6	-56.2	-55.8	-55.4	-55.0	-54.5	-54.1	-53.6	-53.0	-52.5	-51.9	-51.3	-50.7	-50.1	-49.4
350.0	119.1	120.1	120.3	120.6	120.9	121.2	-58.5	-58.1	-57.7	-57.3	-56.9	-56.5	-56.0	-55.5	-55.0	-54.4	-53.8	-53.3	-52.6	-52.0	-51.3
354.0	117.2	118.2	118.4	118.7	119.0	119.3	-60.4	-60.0	-59.7	-59.3	-58.8	-58.4	-57.9	-57.4	-56.9	-56.3	-55.8	-55.2	-54.5	-53.9	-53.2
358.0	115.3	116.3	116.5	116.8	117.1	117.4	-62.3	-62.0	-61.6	-61.2	-60.7	-60.3	-59.8	-59.3	-58.8	-58.2	-57.6	-57.0	-56.4	-55.8	-55.1

• μ versus I_{low}, I_{high} in SNAKE 1 (currents : +/-/+/-). For SNAKE 2 (currents : -/+/-/+) reverse μ sign.

Ilow: / Ihigh	60.0	64.0	68.0	72.0	76.0	80.0	84.0	88.0	92.0	96.0	100.0	104.0	108.0	112.0	116.0	120.0	124.0	128.0	132.0	136.0	140.0
286.0	149.3	155.5	156.7	158.1	159.6	161.1	162.6	164.3	166.0	167.8	169.7	171.6	173.7	175.7	177.9	179.9	177.6	175.3	172.9	170.4	167.9
290.0	151.5	157.5	158.8	160.1	161.5	163.0	164.6	166.2	167.9	169.7	171.5	173.4	175.4	177.5	179.6	178.2	176.0	173.7	171.3	168.8	166.3
294.0	153.5	159.4	160.7	162.0	163.4	164.9	166.4	168.0	169.7	171.4	173.2	175.1	177.1	179.1	178.8	176.7	174.4	172.1	169.8	167.4	164.9
298.0	155.5	161.3	162.5	163.8	165.2	166.6	168.1	169.7	171.4	173.1	174.9	176.7	178.6	179.4	177.3	175.2	173.0	170.7	168.4	166.0	163.6
302.0	157.4	163.1	164.3	165.6	166.9	168.3	169.8	171.3	172.9	174.6	176.4	178.2	179.9	178.0	175.9	173.8	171.7	169.5	167.2	164.8	162.4
306.0	159.2	164.8	166.0	167.2	168.5	169.9	171.3	172.8	174.4	176.1	177.8	179.6	178.6	176.7	174.7	172.6	170.5	168.3	166.1	163.8	161.4
310.0	161.0	166.4	167.5	168.7	170.0	171.3	172.8	174.2	175.8	177.4	179.1	179.2	177.4	175.5	173.5	171.5	169.5	167.3	165.1	162.8	160.5
314.0	162.6	167.9	169.0	170.2	171.4	172.7	174.1	175.5	177.0	178.6	179.7	178.0	176.3	174.4	172.5	170.6	168.5	166.4	164.3	162.0	159.7
318.0	164.1	169.3	170.3	171.5	172.7	174.0	175.3	176.7	178.2	179.7	178.7	177.0	175.3	173.5	171.6	169.7	167.7	165.7	163.6	161.4	159.1
322.0	165.6	170.5	171.6	172.7	173.9	175.1	176.4	177.8	179.2	179.3	177.8	176.1	174.5	172.7	170.9	169.0	167.1	165.1	163.0	160.9	158.7
326.0	166.9	171.7	172.7	173.8	174.9	176.1	177.4	178.7	179.9	178.5	177.0	175.4	173.8	172.1	170.3	168.5	166.6	164.6	162.6	160.5	158.4
330.0	168.1	172.7	173.7	174.8	175.9	177.0	178.2	179.5	179.2	177.8	176.3	174.8	173.2	171.5	169.8	168.1	166.2	164.3	162.4	160.3	158.3
334.0	169.2	173.7	174.6	175.6	176.7	177.8	179.0	179.8	178.5	177.2	175.8	174.3	172.8	171.2	169.5	167.8	166.0	164.2	162.3	160.3	158.3
338.0	170.2	174.5	175.4	176.3	177.4	178.4	179.6	179.3	178.0	176.7	175.4	174.0	172.5	170.9	169.3	167.7	166.0	164.2	162.3	160.4	158.5
342.0	171.1	175.2	176.0	176.9	177.9	178.9	180.0	178.9	177.7	176.4	175.1	173.8	172.3	170.9	169.3	167.7	166.1	164.3	162.6	160.7	158.8
346.0	171.9	175.7	176.5	177.4	178.3	179.3	179.7	178.6	177.4	176.3	175.0	173.7	172.3	170.9	169.5	167.9	166.3	164.7	162.9	161.2	159.3
350.0	172.5	176.2	176.9	177.8	178.6	179.6	179.5	178.4	177.4	176.2	175.0	173.8	172.5	171.1	169.7	168.3	166.7	165.1	163.5	161.8	160.0
354.0	173.0	176.4	177.2	178.0	178.8	179.7	179.4	178.4	177.4	176.3	175.2	174.0	172.8	171.5	170.2	168.8	167.3	165.8	164.2	162.5	160.8
358.0	173.4	176.6	177.3	178.0	178.8	179.6	179.5	178.6	177.6	176.6	175.5	174.4	173.3	172.0	170.7	169.4	168.0	166.5	165.0	163.4	161.8

3.3 Orbit compensation

We comment here on a noticeable effect on spin rotation, over the beam line segment comprising the snake and the orbit correctors, induced by the vertical orbit centering and horizontal orbit compensation at the snake.

In the preceding sections RHIC snake is taken isolated. Fig. 11 shows that the snake introduces a noticeable (≈ 0.1 mm) horizontal dipole defect (in and out coordinates are different). The effect is much weaker for the vertical motion. However, once combined with the vertical centering of the reference orbit on the snake axis by vertical correctors, the compensation of that horizontal dipole defect by horizontal correctors causes the spin rotation to depart from 180^o over the snake+correctors beam line segment.

This is illustrated in Fig. 17 which shows the orbit effect (mostly horizontal) of the snake taken isolated (snake currents are nominal here, for $(\mu,\phi) = (180, \pm 45)$ degree at 250 GeV), and in Fig. 18 which gives the spin rotation through RHIC snake+correctors segment (here, in Blue, 95.8 m from "BI9_QF11" quadrupole to "BI9_TV4" vertical corrector, including snake 1). That beam line segment encompasses two vertical correctors upstream of the snake, for vertical centering of the helical trajectory on the snake axis, as well as two horizontal and two vertical correctors downstream of the snake, to respectively locally close the vertical orbit bump and compensate the snake induced horizontal dipole effect. Two arrangements of the downstream correctors are assessed, namely HVHV (interleaved) and VVHH. The latter configuration (vertical bump closed prior to horizontal dipole compensation) minimizes the departure from 180^o spin rotation over the snake+corrector segment.

This non-180^o spin rotation causes a small tilt of the periodic stable precession axis $\vec{n}_0$ from vertical around the ring, this is discussed further in Sec. 4.

4 In RHIC

This Section re-visits RHIC in the presence of the snakes, using their OPERA field maps, and in some cases, for the sake of comparison with field map outcomes, using instead a pure spin rotation, exempt of any orbital effect ("`SPINR`" keyword in Zgoubi [13]).

The OPERA model is the optimized 4-map one, with OPERA currents $I_{low} = 93.6\ A,\ I_{high} = 322.9\ A$ ensuring $(\mu,\phi) = (180, \pm 45)$ in the 250 GeV region, Sec. 3.2 and Fig. 16.

Optics and polarization parameters obtained from ray-tracing assume a defect-free ring, including the local vertical orbit bumps at the snakes, and including or not, as specified in due place, the vertical orbit separation bumps at the 6 IPs. These optics working conditions are summarized under the form of figures, at injection pp. 15-16, and at store pp. 17-19.

Tab. 4 details the basic optical parameters and spin motion properties using snake field maps (some results with `SPINR` instead are also given for comparison). Three things to note there, regarding the use of the field map snake model :

- snake angles are optimized for store energy, and therefore not exactly $\mu = 180$ deg, $\phi = \pm 45$ deg at injection (the latter a source of spin tune shift $\Delta Q_{\rm sp} = \frac{\phi_{\rm snake_1} - \phi_{\rm snake_2}}{\pi}$),

- the snake induces a small horizontal dipole effect (Fig. 17). Compensating it with nearby correctors induces a small tilt of the stable spin precession direction, Sec. 3.3 and Fig. 18.

- under the effect of the vertical positioning of the orbit at snake entrance (for centering in the high-field helix modules) and of the local compensation of the horizontal orbit defect, the spin rotation is slightly changed compared to the isolated snake case.

Tab. 5 details the spin components and in particular the vertical tilt, at IP6, IP8, H-jet and pC polarimeters. It can be observed that the periodic spin precession direction is not vertical, with in particular a 3.84 degree tilt (resp. 2.06 deg) at IP6 and IP8 at injection (resp. at store, in spite of the perfect setting of the two snakes at that energy). The bulk of the effect at 250 GeV stems from the x-rotation in the vertical steerers used to close the vertical bumps at the snakes. At injection energy the effect of non-nominal snake angles $\mu = 179.79$, $\phi = \pm 45.22$ (see Tab. 4) adds to the latter. The rightmost column in Tab. 4 also shows an small effect on spin tune, greater in the 250 GeV modeling. A way to avoid this would be for the optimization of the snake currents, for $\mu = 180$ deg, $\phi = \pm 45$ deg setting, to encompass the vertical orbit bump at the snake.

4.1 Injection optics

Injection optics used here is derived from Run 17 files, obtained from translation of RHIC model in MADX (note that K1 and K2 indices in the bends are set to zero in Zgoubi).

Note that the magnetic field sign in the snake determines the sign of the orbit. The present +/-/+/- and -/+/-/+ current signs in the 4 modules of respectively snake 1 and snake 2 (clockwise from IP6 in Blue) yield identical orbit bump at the snakes (Fig. 19) to that measured during RHIC operation, and as obtained from MADX Run 17 model as well (Fig. 27). This is considered to validate the snake current signs in the present field map based simulations.

Table 4: Optical parameters, snake angles and spin tune $Q_{\rm sp}$, at injection and at store, using snake field maps ("OPERA" rows). Results with pure-rotation snake model ("SPINR" rows) are also given for comparison. The rightmost two columns give, respectively, the actual difference between between the closed orbit angles at the snakes in the Zgoubi model, and the expected perturbation it induces on spin tune, $\delta Q_{\rm sp}$.

	orbit length (m)	wave numbers Q_x	Q_y	chromaticities ξ_x	ξ_y	γ_{tr}	μ	ϕ	$Q_{\rm sp}$	$\lvert\Delta x'\rvert$ (mrad)	$\frac{2G\gamma\lvert\Delta x'\rvert}{\pi}$
Injection, Run 17 optics, no IP bumps (Figs. 19-22)											
SPINR	3833.8422	28.690	29.680	52.2	54.0	22.6574	180	± 45	0.49977	≈ 0	0
OPERA	3833.8462 (δ =4 mm)	28.687	29.743 (δ =0.063)	68.5	55.1	22.6577	179.79	± 45.22	0.49987	2.5	0.073
250 GeV, Run 17 optics, no IP bumps (Figs. 29, 30)											
SPINR	3833.84153	28.685	29.675	21.3	23.6	23.7778	180	± 45			
OPERA	3833.84157 ($\delta = 0.04$ mm)	28.685	29.676 ($\delta = 10^{-3}$)	21.3	23.6	23.7778	$\approx$180	± 45	0.48248		
255 GeV, pp11v7 optics, with IP orbit bumps (Figs. 33-35)											
OPERA	3833.8415	28.685	29.674	2.1	2.1	23.8345	$\approx$180	± 45	0.50000		

Table 5: $\vec{n}_0$ vertical tilt value, at various locations along the ring at injection and at store, in the presence of the snakes at nominal setting $(\mu,\phi) = (180, \pm 45)$. Snakes are represented either using their OPERA field maps, or using a pure, theoretical, spin rotation. The "Maximum tilt" indicated excludes the regions of the snakes.

	Tilt of $\vec{n}_0$ with respect to vertical (deg.)		
	Using snake field maps		Using pure rotation
	IP bumps zero-ed	IP bumps set	IP bumps set
Injection, Run 17 optics			
Injection kicker	3.84	2.59	2.7
H-jet	1.12	1.42	1.5
pC polrmtr	1.12	1.37	1.5
Maximum tilt	3.84	4	4.3
Refer to figure :	*24*	*26*	*28*
250 GeV, Run 17 optics			
IP6	1.92		0.25
IP8	1.92		0.33
H-jet	2.35		0.22
pC polrmtr	2.35		0.75
Maximum tilt	2.35		17
Refer to figure :	*32*		*39*
255 GeV, pp11v7 optics			
IP6		2.81	
IP8		2.92	
H-jet		1.44	
pC polrmtr		3.87	
Maximum tilt		18	
Refer to figure :		*37*	

4.1.1 Using snake field maps, IP bumps zero-ed

The results are summarized in a series of figures :
- Fig. 19 : H and V orbits are zero except at the snakes, where they are as displayed in Fig. 9, centered on the high field helix axis,
- Fig. 20 : optical functions in the Zgoubi model, using snake OPERA maps (they are identical to the MADX model, this goes without saying),
- Fig. 22 : a zoom on the IP6-IP8 region, showing marginal effect of the snake fields on the paraxial horizontal focusing,
- Fig. 21 : a zoom on the IP6-IP8 region, showing significant effect of the snake fields on the paraxial vertical focusing, inducing a change in the vertical tune Q_y (col. 4, rows 4, 5 in Tab. 4),
- Figs. 23, Fig. 24 : the former displays the longitudinal, n_l, and transverse horizontal, n_x, components of the periodic precession axis $\vec{n}_0$ around RHIC. They are not zero : $\vec{n}_0$ is tilted with respect to the vertical axis, with the snakes determining essentially two regions with respectively 3.84 degrees and 1.12 degree tilt, Fig. 24 and Tab. 5.

This tilt of $\vec{n}_0$ is correlated to the orbit bump at the snake, to its compensation, and to the actual spin tilt by the snake, $\mu \approx 180$ deg., as discussed earlier (Sec. 3.3 and Figs. 16, 17, 18).

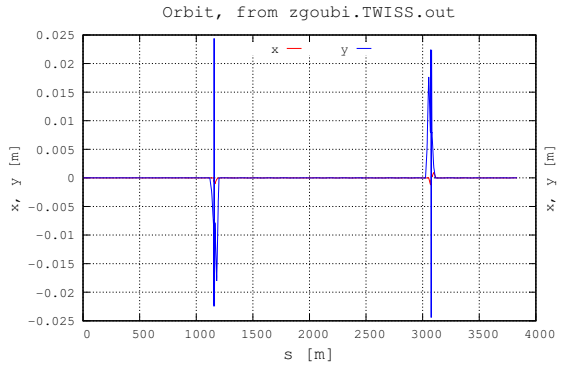

Figure 19: Snake induced orbit in RHIC is cancelled using upstream and downstream orbit correctors, essentially vertical.

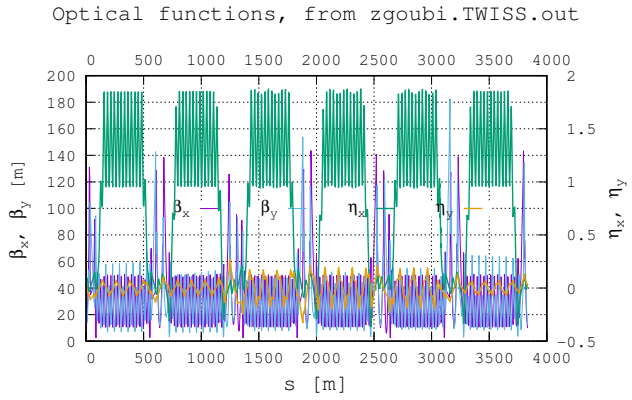

Figure 20: Optical functions in RHIC at injection, with snakes. Vertical plane is slightly perturbed by the snakes, see Figs. 21 ,22.

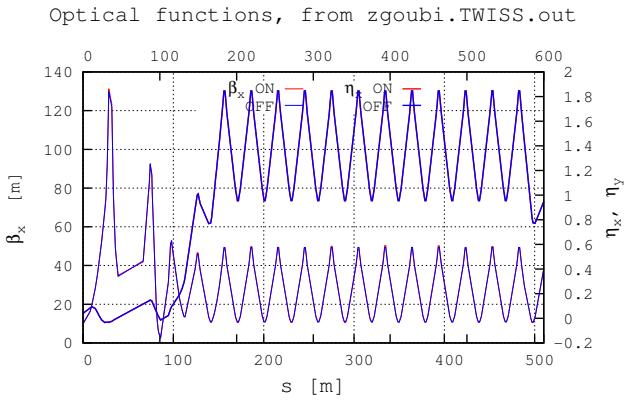

Figure 21: IP6-IP8 region of the horizontal optical functions in RHIC at injection, with and without snakes.

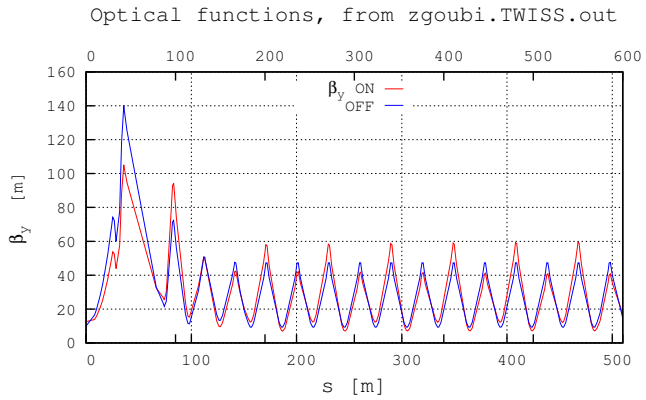

Figure 22: IP6-IP8 region of vertical optical functions in RHIC at injection, with and without snakes.

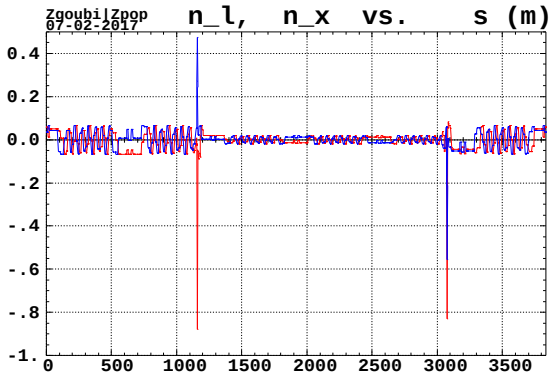

Figure 23: Horizontal components n_l (red), n_x (blue) of the stable spin precession axis $\vec{n}_0$ around RHIC Blue. Snake settings are optimal for 250 GeV (as in Fig. 16).

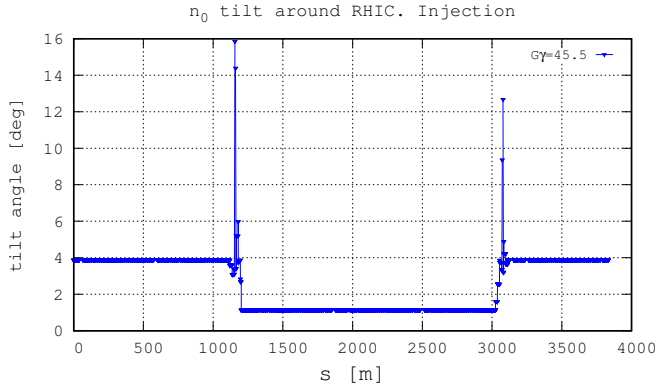

Figure 24: Vertical tilt of $\vec{n}_0$ around RHIC resulting from the orbit bump at the snakes, their compensation, and the actual μ value at injection.

4.1.2 Using snake field maps, IP bumps set

Compared to the previous Section, vertical orbit separations at IPs are added. The brute translation from MADX RHIC Run 17 model used here results in a slight residual orbit, in both planes (Fig. 25), which we choose to live with, as it is small. OPERA maps are used, the orbit is centered on snake axis at the snakes prior to installing the snake sections in that model.

Fig. 26 shows, as in the previous IP bump-free case (Fig. 24), essentially two regions of V-tilt values, yet now with additional local extrema, in the regions of the rise and fall of the IP separation bumps. The particular values of $\vec{n}_0$ tilt at the injection kicker, H-jet and pC polarimeter can be found in Tab. 5.

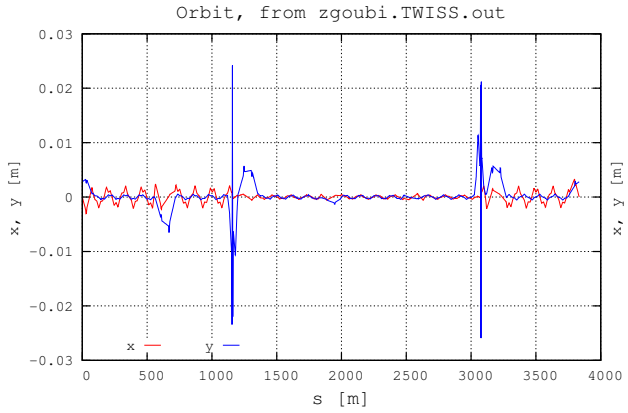

Figure 25: H and V orbits in RHIC at injection, Run 17 optics model. Snakes field maps are used here.

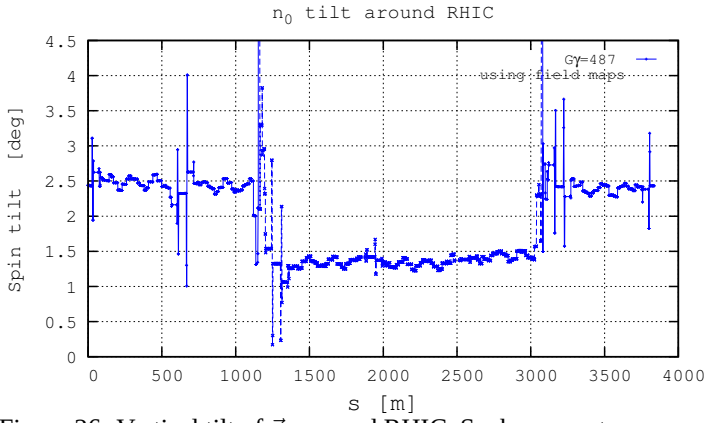

Figure 26: Vertical tilt of $\vec{n}_0$ around RHIC. Snake currents are nominal for 255 GeV so resulting at injection in $\phi = \mp 45.22$ deg. in respectively snake 1, 2, and $\mu = 179.84$ deg. (*cf.* Fig. 16, for $G\gamma = 45.5$). The $\vec{n}_0$ tilt extrema of about 14 deg at the two snakes have been cut out.

4.1.3 Using theoretical spin rotation, IP bumps set

This simulation uses the 'SPINR' keyword in Zgoubi, a pure spin rotation, to represent the snakes (no orbital effect), instead of field maps. The model used is the same as in Sec. 4.1.2, only the snakes have been replaced by 'SPINR' on the one hand, and on the other hand the local orbit bump at the snake locations is that from the MADX model, $i.e.$, artificially built using local correctors (*not* resulting from snake fields, as these are absent). IP bumps are in place as well (Fig. 27).

Snake angles are nominal here, $\phi = \mp 45$ deg. in respectively snake 1, 2, and $\mu = 180$ deg. $\vec{n}_0$ behavior, Fig. 28, comes out *quantitatively close* to the field map case (Fig. 26), which indicates that the $\vec{n}_0$ vertical tilt observed here results from the presence IP bumps : this is the effect discussed in Sec. 3.3, Fig. 18. This is corroborated by the store energy case, Fig. 39, where the absence of orbit bumps at the snakes in the MADX model (residual orbit bumps at the snakes are small at store, not subject to local compensation Fig. 38)

The particular values of $\vec{n}_0$ at injection kicker, H-jet and pC polarimeter can be found in Tab. 5.

For the sake of completeness, injection snake angles $\phi = \mp 45.22$ deg. in respectively snake 1, 2, and $\mu = 179.84$ deg. of the field map case (see $G\gamma = 45.5$ region in Fig. 16) have also been simulated, a case not shown here, however the effect on $\vec{n}_0$ and its local extrema appears to be marginal.

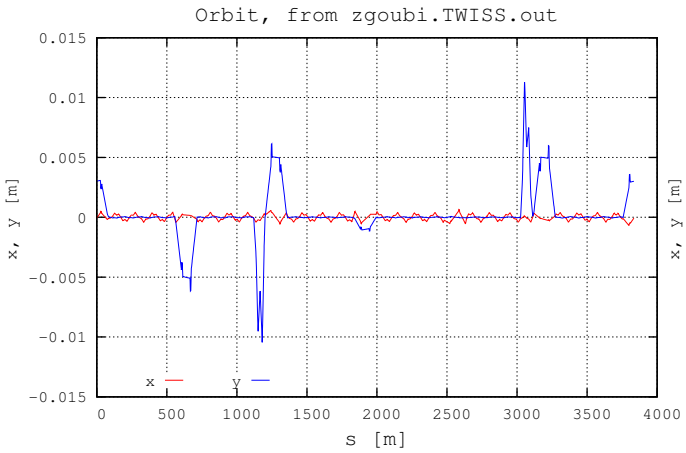

Figure 27: H and V orbits in RHIC at injection, Run 17 optics model. Snakes are theoretical spin rotators here - not field maps.

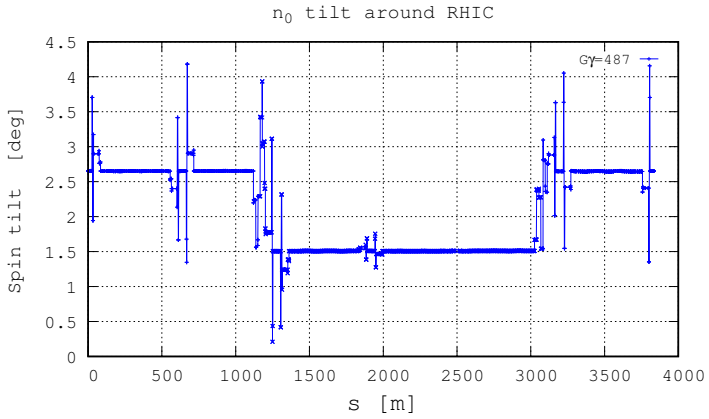

Figure 28: Vertical tilt of $\vec{n}_0$ around RHIC. Snake angles are nominal here, $\phi = \mp 45$ deg. in respectively snake 1, 2, and $\mu = 180$ deg. Note that changing to $\phi = \mp 45.22$ deg. in respectively snake 1, 2, and $\mu = 179.84$ deg. instead, as in the field map case (Sec. 4.1.2 and Fig. 16 at $G\gamma = 45.5$) has marginal effect on $\vec{n}_0$. Note that, compared to Fig. 26, the local $\vec{n}_0$ tilt extrema of about 14 deg at the two snakes are absent, as SPINR is used here.

4.2 Store optics

4.2.1 Using snake field maps, IP bumps zero-ed

Store optics used here, 250 GeV, is derived from Run 17 MADX files, the main difference is in K1 and K2 indices in RHIC main bends set to zero. In the present case, orbit bumps at IPs have been zero-ed.
The particular values of $\vec{n}_0$ tilt at IP6, IP8, H-jet and pC polarimeter can be found in Tab. 5.

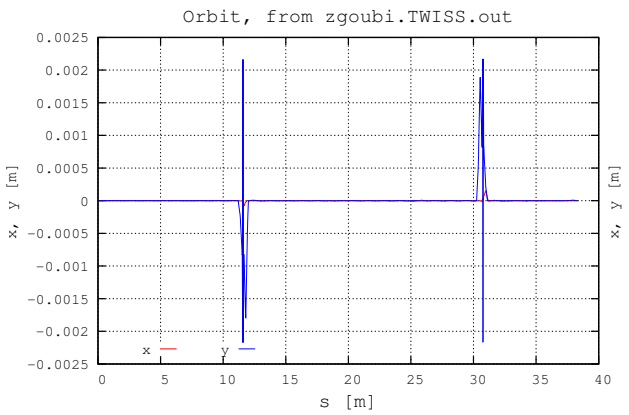

Figure 29: Snake induced orbit in RHIC is cancelled using upstream and downstream orbit correctors, essentially vertical.

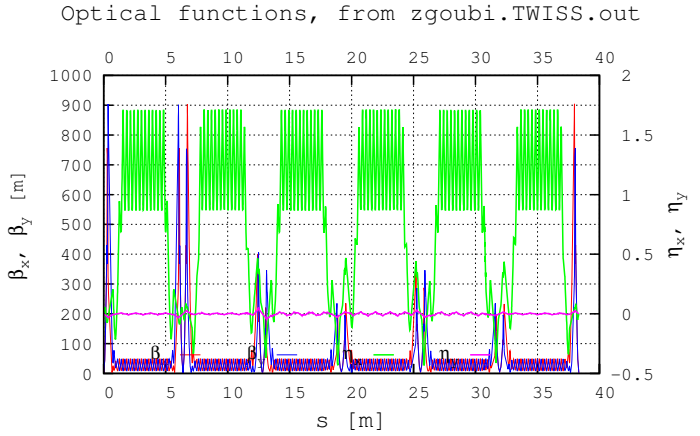

Figure 30: Optical functions in RHIC at store, with snakes.

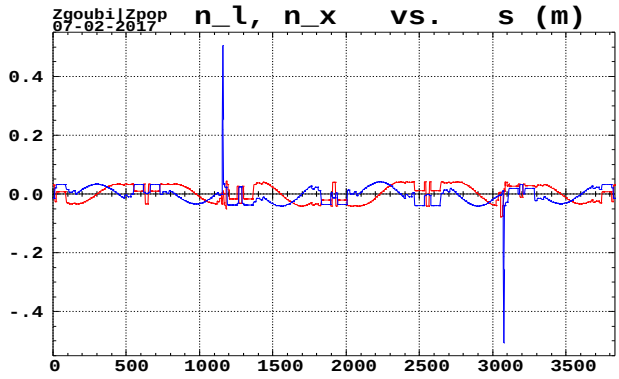

Figure 31: Horizontal components S_l (red), S_x (blue) of the stable spin precession axis $\vec{n}_0$ along RHIC, store optics, case of optimal snake settings (as in Fig. 16).

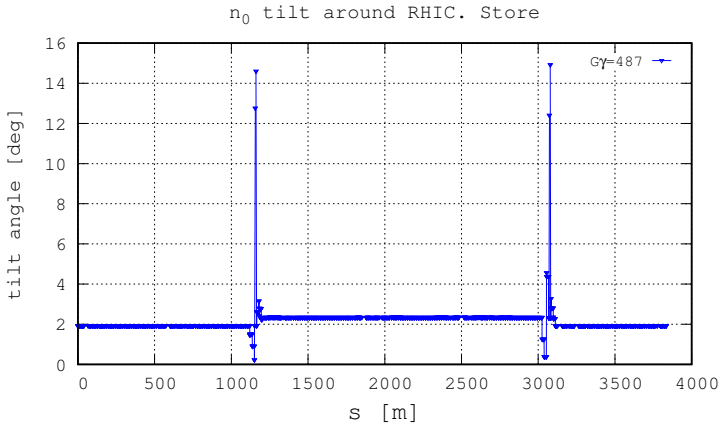

Figure 32: Vertical tilt of $\vec{n}_0$ around RHIC, case of interleaved snake bump corrector scheme.

4.2.2 Using snake field maps, pp11v7 optics

The store optics considered here, 255 GeV ($G\gamma = 487$), is derived from pp11-v7 MAD model, already used in the past in several investigations regarding polarization transport in RHIC [12]. A difference compared to the previous section is that it includes a 25 μm random orbit, in both horizontal and vertical planes (this however has marginal impact on $\vec{n}_0$). The orbit separation at IPs induces local extrema of $\vec{n}_0$ at the rise and fall of the bumps. The particular values of $\vec{n}_0$ tilt at H-jet and pC polarimeter can be found in Tab. 5.

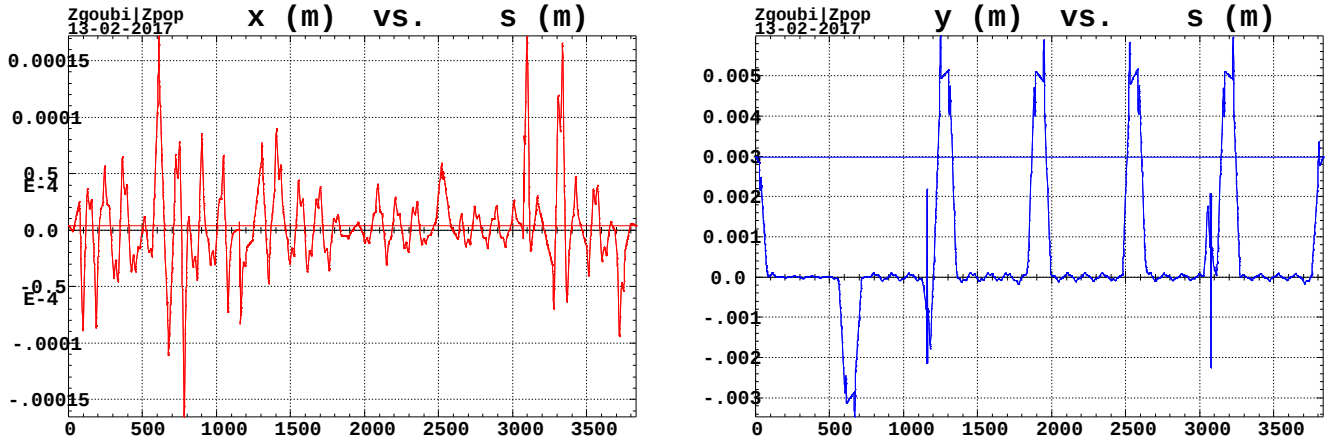

Figure 33: Horizontal and vertical orbits in RHIC. The orbit bumps at the snakes are apparent at ∼1150 m and ∼3100 m.

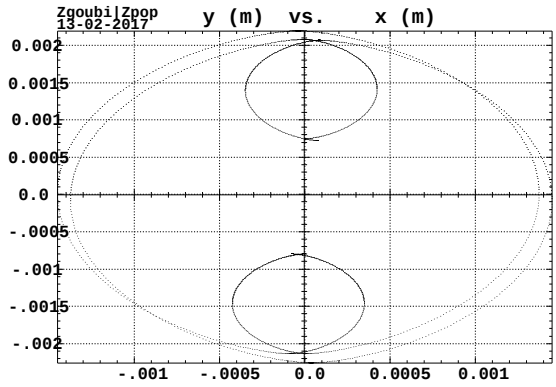

Figure 34: Nominal orbit centering in the high-field helix modules in both snakes.

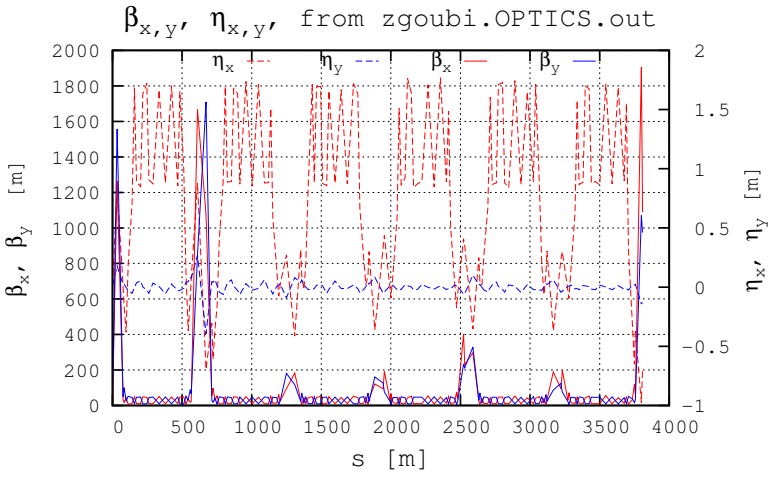

Figure 35: Optical functions in RHIC at store, with snakes.

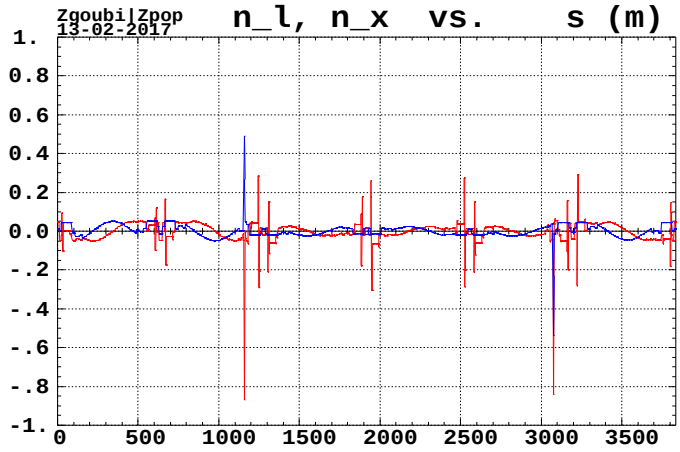

Figure 36: Horizontal components S_l (red), S_x (blue) of the stable spin precession axis $\vec{n}_0$ along RHIC, store optics, case of optimal snake settings (as in Fig. 16).

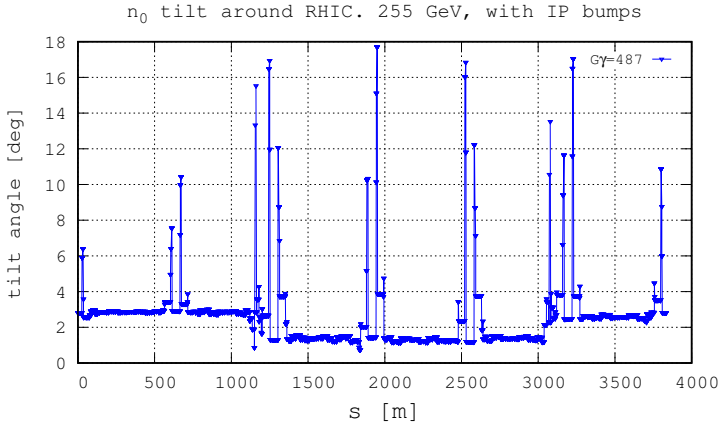

Figure 37: Vertical tilt of $\vec{n}_0$ around RHIC, case of interleaved snake bump corrector scheme. Note that the vertical tilt of $\vec{n}_0$ exceeds 16 degrees locally, in the region of IPs 10, 12, 2 and 4.

4.2.3 Using theoretical spin rotation, IP bumps set

This simulation uses the 'SPINR' keyword in Zgoubi to simulate a pure spin rotation by the snakes (no orbital effects), instead of the latters' 3-D field maps. The vertical orbit centering bumps at the snakes are zero in the store energy Run 17 MADX model (Fig. 38), as the residual orbit induced by the snakes is considered negligible. IP bumps are in place (Fig. 38).

Compared to Sec. 4.2.2, $\vec{n}_0$ tilt is quasi-zero in the arcs (not exactly zero due to residual vertical orbit) as SPINR does not introduce any orbit effect so avoiding the interleaved H/V orbit compensation effect discussed in Sec. 3.3 (Figs. 17, 18). Local extrema of $\vec{n}_0$ are present at the rise and fall of IP separation bumps. The particular values of $\vec{n}_0$ tilt at H-jet and pC polarimeter can be found in Tab. 5.

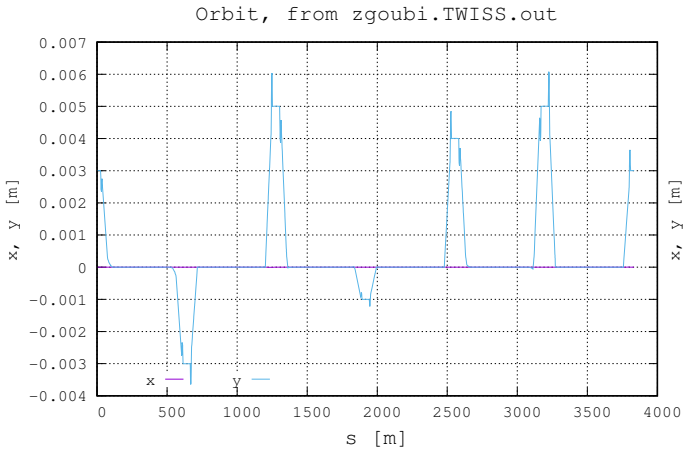

Figure 38: H and V orbits in RHIC at store, Run 17 optics model. Snakes are theoretical spin rotators here - not field maps.

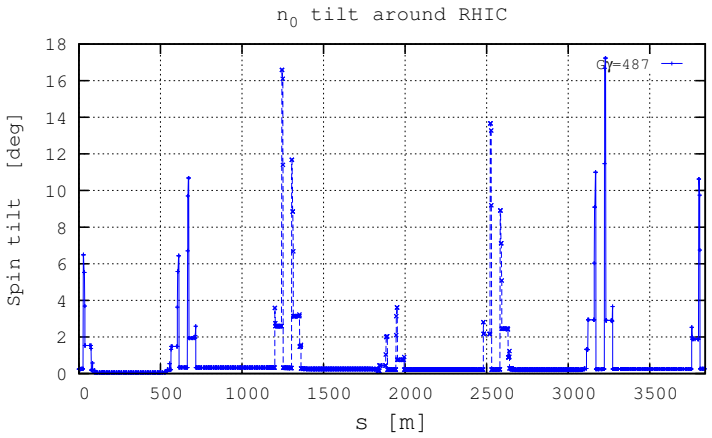

Figure 39: Vertical tilt of $\vec{n}_0$ around RHIC. Snake angles are nominal, $\phi = \mp 45$ deg. in respectively snake 1, 2, and $\mu = 180$ deg.

5 Conclusion

Spin dynamics in RHIC is modeled using OPERA field maps to represent the helical snakes. This allows detailed insight into optical and polarization parameters, including orbit, focusing and periodic spin precession axis.

Modeling the snakes in RHIC by means of their field maps shows that the stable spin direction around the ring is titled by $2 \sim 4$ degrees, depending on the location, energy (injection, store) and on the vertical orbit centering scheme at the snakes.

One goal of this work was to develop the necessary material for assessing a possible origin of the up to 16 degrees tilt measured at the pC CNI at store in RHIC Blue ring. Preliminary investigations have shown that orbit defects, snake current mis-settings, or momentum offset, cannot explain such strong tilt as it would require these to be prohibitively large. This will be subject to further investigation.

APPENDIX

A Longitudinal position of the snake in the field map frame

In the full-snake single map, the vertical central-plane symmetry of the 4-module set happens to be slightly shifted with respect to the origin of the field map, which has been taken at the center of the map mesh, Fig. 40.

This can be taken into account if desired in positioning the field map in the RHIC optical sequence. We chose here to ignore that instead, as spin does not rotate in a drift space.

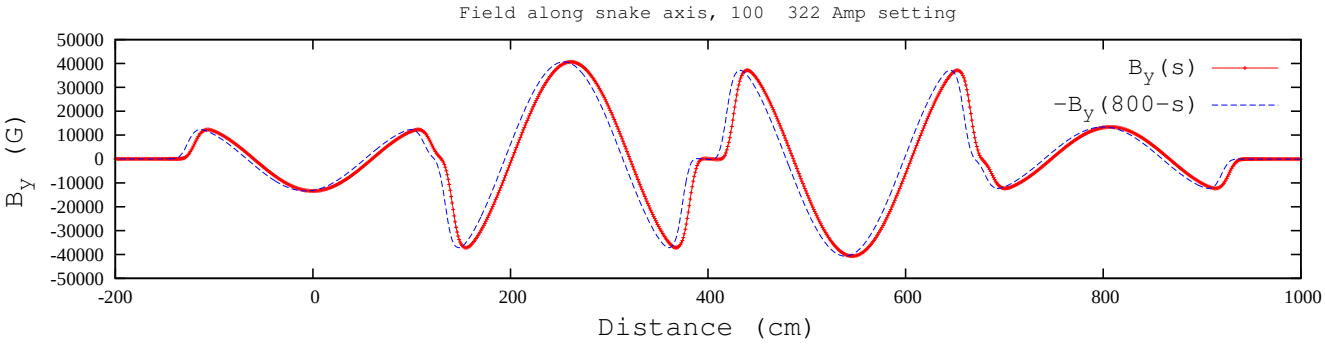

Figure 40: Vertical field component along RHIC snake axis, OPERA map. Plotting the forward ($B(z)$) and backward ($-B(800-z)$) field distributions shows a $\approx$ 35 mm shift (half the distance between any two neighboring peaks), to the right, of the 4-module set vertical field symmetry plane with respect to the center of the field map.

B "Splitted full-snake" OPERA model in zgoubi

The following is the input data file to zgoubi, for the optimization of, independently of one another, the low- and high-field values in the four separate regions of the single-map full-snake OPERA model. The method is based on the use of the 'droite de coupure' technique in zgoubi [13, see the Index].

It can be seen that only one field map, the full-snake map, is advocated in the data list. The 'droite de coupure' method allows defining a limited integration region within the map, namely, between two vertical planes defined by their intersection (the 'droite de coupure') with the median plane.

The resulting particle motion, field and spin components across the snake are displayed in Figs. 40, 42.

```
'OBJET'
853.71244451829796e3  ! E_kin=255   Gg=489.   ! 79.366774592048841e3       ! 45.5
1
3  1 1 1 1 1
   0.000000E+00   0.000000E+00   0.000000E+00   0.000000E+00   0.00  0.000000E+00
   0.00000000E+00   0.00000000E+00  -8.15622346E-02   0.00000000E+00   0.00  1.00000000E+00

'PARTICUL'
9.3827203E+02 1.602176487E-19 1.7928474 0 0
'SPNTRK'
4
  1.00000000 0. 0.00000000
  0.00000000 1. 0.00000000
  0.00000000 0. 1.00000000

'TOSCA'      lowB
0  0  !! 20
  9.45040160E-04  1.00000000E+00  1.00000000E+00  1.00000000E+00
HEADER_8
1201 41 41  15.1  1.
b_model4hel-a5-100A-322A-06-dec-2016-x-4_4_y-4_4_z-200_1000-integralPatched.table
1 1. 0 -130.
2
.1
2   0.00000000E+00  0.00000000E+00  0.00000000E+00
'DRIFT'
-870.      ! = 1000 - 130

'SPNPRT'   MATRIX

'DRIFT'
-330.      ! = 200 + 130
'TOSCA'      highB
0  0  !! 20
  1.04410391E-03  1.00000000E+00  1.00000000E+00  1.00000000E+00
HEADER_8
1201 41 41  15.1  1.
b_model4hel-a5-100A-322A-06-dec-2016-x-4_4_y-4_4_z-200_1000-integralPatched.table
2 1. 0 -130. 1. 0 -400.
2
.1
2   0.00000000E+00  0.00000000E+00  0.00000000E+00
'DRIFT'
-600.           ! = 1000 - 400

'SPNPRT'   MATRIX
```

```
'DRIFT'
-600.           ! = 200 + 400
'TOSCA'     -highB
0  0  !! 20
  1.04410391E-03  1.00000000E+00  1.00000000E+00  1.00000000E+00
HEADER_8
1201 41 41  15.1  1.
b_model4hel-a5-100A-322A-06-dec-2016-x-4_4_y-4_4_z-200_1000-integralPatched.table
2 1. 0 -400. 1. 0 -677.2
2
.1
2   0.00000000E+00  0.00000000E+00  0.00000000E+00
'DRIFT'
-322.8           ! = 1000 - 677.2

'SPNPRT'   MATRIX

'DRIFT'
-877.2           ! = 200 + 677.2
'TOSCA'     -lowB
0  0  !! 20
  9.45040160E-04  1.00000000E+00  1.00000000E+00  1.00000000E+00
HEADER_8
1201 41 41  15.1  1.
b_model4hel-a5-100A-322A-06-dec-2016-x-4_4_y-4_4_z-200_1000-integralPatched.table
2 1. 0 -677.2  1. 0. -1000
2
.1
2   0.00000000E+00  0.00000000E+00  0.00000000E+00

  'FIT'
  3
  1  42   0      [-3,3]
  5  10 20.010   .5
  10  10 15.010   .5
  4   1D-10  9999
  7.3 1 4 10  0.    1.   0
  10.2 1 1 #End   3.14159265359 1. 0
  10.3 1 1 #End   0.7071 1. 0
  10.3 1 2 #End  -0.7071 1. 0

'SPNPRT'   MATRIX  PRINT

!'REBELOTE'
! 60 0.1 0 1
! OBJET 45   .093:1.

'END'
```

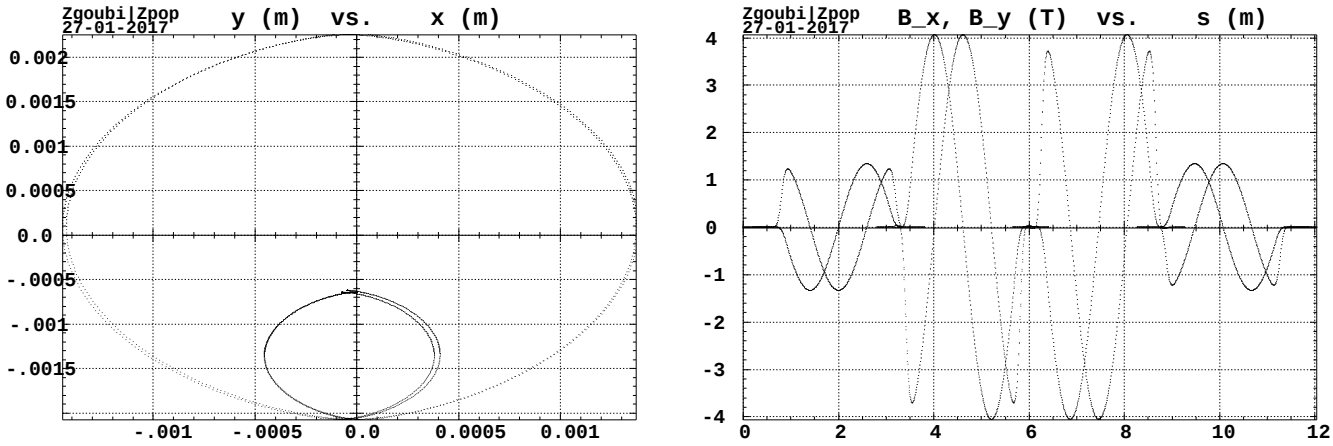

Figure 41: Left : a superimposition of the projection of the helical motion in the transverse plane (the small helical trajectory is along the low-field modules) obtained from, on the one hand the 4-piece splitted 12 m extent full-snake field map, and on the other hand the 4-map assembly. Right : a superimposition of the B_x and B_y field components along the helical trajectory in the previous two cases. Maximum field amplitudes have been normalized to the same values in both cases, 1.337 T (low field) and 4.065 T (high field).

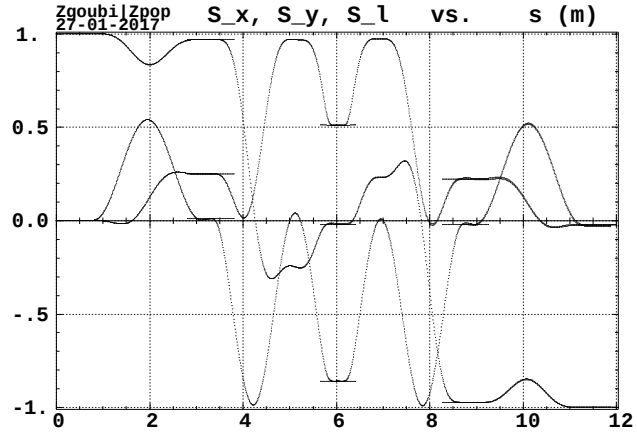

Figure 42: Spin motion at 255 GeV through, superimposed, on the one hand the 4-piece splitted full-snake OPERA map, on the other hand the 4-map assembly, both with fields as of OPERA computation (prior to any fine tuning). Starting spin is vertical, $(S_x, S_y, S_l) = (0, 1, 0)$. Matrix computation from spin transport yields close results, namely, in the first case : spin rotation $\mu = 178.159$ deg, precession axis at -44.064 deg from longitudinal, in the second case : spin rotation $\mu = 177.477$ deg, precession axis at -44.522 deg.

References

[1] Spin dynamics in AGS and RHIC, W. W. MacKay et al., PAC 2003.

[2] Exploring a Possible Origin of an Abnormal $10 \backsim 15$ degree Spin Tilt Observed at RHIC Polarimeters, F. Méot, R. Gupta, H. Huang, V. Ranjbar, W. Schmidke, SPIN'16 Conf., Champaign, IL, USA (2016).

[3] See BNL C-AD Tech Note and Spin Note repositories,
http://public.bnl.gov/docs/cad/Pages/Home.aspx,
http://www.agsrhichome.bnl.gov/RHIC/Spin/spinnotes/snlist.html.

[4] M. Okamura, Three dimensional field analysis of helical snake magnets for RHIC, AGS/RHIC/SN 030 (June. 1996).

[5] A. Luccio, Optimization of spin angles from a helix field map, AGS/RHIC/SN 042 (Nov. 1996).

[6] Helical Magnets, *in The RHIC Magnet System*, M. Anerella et al., Nuclear Instrum. Meth. A 499 (2003) 280-315.

[7] Hybrid helical snakes and rotators for RHIC, E. Courant, Spin Note SN10 (Jan. 1996).

[8] Path Length through Helical Snakes and Rotators, W. MacKay, Tech Note BNL C-A/AP/140 (2004).

[9] Helical Partial Snakes for the AGS, T. Roser et al. AGS/RHIC/SN 072

[10] The ERL-based Design of Electron-Hadron Collider eRHIC V. Ptitsyn et al.,
accelconf.web.cern.ch/AccelConf/ipac2016/papers/wepmw027.pdf.

[11] MAD8 to Zgoubi, and MADX to Zgoubi translators are available at $/rap/lattice\_tools/zgoubi/tools$

[12] Spin Meeting Minutes, http://www.cadops.bnl.gov/AP/spinmeeting.htm

[13] Zgoubi Users' Guide, F. Méot, Tech. Note CA-AP/ (2012), Rep. BNL-98726-2012-IR.
https://www.osti.gov/scitech/biblio/1062013-zgoubi-users-guide

[14] Y.A. Anferov, Helical snakes with no orbit correction and their discrete analogues, Part. Acc. Vol. 48, pp. 61-73 (1994).

[15] Exploring a possible origin of a 14 deg y-normal spin $\vec{n}_0$ tilt at RHIC polarimeter, F. Méot, H. Huang, Tech Note BNL C-A/AP/538 (2015).